

CHARLES UNIVERSITY

Faculty of Mathematics and Physics



**Novel routes for nanoparticle synthesis using gas
aggregation sources and the study of nanoparticle
interaction with substrates**

Habilitation Thesis

RNDr. Pavel Solař, Ph.D.

Prague 2023

Acknowledgment

I wish to express my gratitude to the individuals who have supported me throughout the completion of this thesis and who have contributed to meaningful discussions and provided valuable feedback, enhancing the quality of my work. Their assistance and encouragement have played a significant role in shaping my academic progress.

I would like to specifically thank to Ondřej Kylián, whose valuable insights improved much of my work and led to better written papers, to my student Kateřina Škorvánková, who did immense amount of high precision lab work, to Jan Hanuš for his invaluable technical advice, to Jaroslav Kousal and Suren Ali-Ogli for their help with calculations and to Oleksandr Polonskyi for all his support during my research fellowship at University of Kiel.

I extend my thanks also to my family for their consistent support and understanding, which has provided a foundation for my pursuit of education.

Contents

1	Introduction	1
2	Preparation of nanoparticles using a gas aggregation source	1
3	Composite nanoparticles	4
3.1	CuW composite nanoparticles from a single target	4
3.2	Titanium/nickel composite NPs from two magnetrons in the same aggregation chamber	9
3.3	Composite metal/plasma polymer NPs	11
4	Measurement of nanoparticles speed	14
4.1	Description of mechanical time-of-flight filter	15
4.2	Processing and deconvolution of measured data	18
4.3	Dependency of NPs speed on mass and aggregation chamber pressure	20
4.4	Dependency of nanoparticles speed on deposition chamber pressure	25
5	Investigation of nanoparticle reflection from substrate	26
6	Conclusions	33
7	References	34
8	List of commented publications	41
9	Commented publications	42

1 Introduction

Results of this work have been achieved during my employment at the Department of Macromolecular Physics, Faculty of Mathematics and Physics, Charles University and partially also during my research fellowship at Christian-Albrechts University at Kiel in the Group of Prof. Franz Faupel.

The preparation of nanoparticles using a gas aggregation source (GAS) has been my scientific interest since my Ph.D. studies. Afterwards, my focus shifted from preparation of single-phase nanoparticles (NPs) to composite ones. Additionally, I studied the transport of NPs from inside of the nanoparticle source to the substrate and investigated the interaction of the nanoparticles with the substrate upon impact.

The first part of this work is devoted to the brief description of the gas aggregation source and to the comparison with other methods of nanoparticles (NPs) production. The second part describes the formation of different types of composite NPs in the gas aggregation source reported in my publications [PS 1], [PS 2], [PS 3], [PS 4]. The next chapter explains the measurement of speed of NPs outside the gas aggregation source and parameters that influence it [PS 5], [PS 6]. The last chapter considers all the information and shows that nanoparticles may reflect from the substrate upon impact with the effect strongly dependent on the nanoparticle type and speed and also on properties of the substrate [PS 7].

2 Preparation of nanoparticles using a gas aggregation source

Nanotechnologies, and specifically nanoparticles represent an important area of current research and find extensive applications in industry. The significance of the nanoparticles stems from their high surface area and unique physical and chemical properties, which arise from their nanoscale dimensions. These attributes grant nanoparticles a range of exceptional characteristics that set them apart from bulk materials, making them crucial for advancements in fields such as materials science, medicine, electronics, energy storage, and environmental remediation [1], [2].

There are numerous methods to prepare nanoparticles that in principle divide into 3 groups: physical, chemical, and biological. The most common are chemical methods that often provide

excellent control over the size and shape of the NPs and allow production in mass quantities. On the other hand, these methods require large amounts of highly toxic precursors and are not very suitable for the production of nanoparticle films. Since the NPs produced by chemical methods are generally formed in volume of a liquid, the NPs require to be extracted from the liquid and dispersed on surface. That is very difficult to do properly since the NPs tend to aggregate on the surface as the solution evaporates and also the solution usually leaves a residue behind.

Similar problems arise with the use of biological methods (e.g. microorganisms assisted biogenesis). Even though these methods can also produce high quality NPs, they suffer from the presence of residues and difficulties with the deposition on substrates.

Physical methods use mechanical pressure, heat, radiation or plasma to cause material to disintegrate, evaporate or condensate to generate NPs. They can be divided on top-down and bottom-up techniques. Top-down processes involve e.g. milling [3], but aside from the fact that they are again volume processes, they also suffer from the poor size and shape distribution. On the other hand, the bottom-up methods start from individual atoms or molecules that are used to build NPs. There are again some volume based methods such as plasmas in liquid with suitable precursor [4], [5]. Methods suitable for nanoparticle films generation include electrospraying [6]–[8], flame spray pyrolysis [9], or techniques using plasma jets [10] and dielectric barrier discharge [11], [12]. A big class of the bottom-up physical methods is based on the condensation of supersaturated vapor or activated organic molecules under vacuum conditions. These processes take place in gas phase and start with introducing vaporized source material that either directly condensate into NPs or the NPs formation is assisted by a chemical reaction. The methods mostly differ in the way how the vaporized source material is introduced and whether some chemically active species are present. The NPs formation in the gas phase has a tremendous advantage when trying to spread them on the surface since there is no liquid residue and no capillary effects-induced aggregation. One of these methods is also the magnetron-based gas aggregation source used in this work e.g [13]–[15]. These and other methods are discussed in detail in review paper by Dhand et al [1].

A gas aggregation source (GAS) for nanoparticles was first constructed by Sattler et al [16] who used an evaporator as the source of the material. Since the evaporator is always rather unstable, difficult to maintain and limited to low melting point materials, it was later replaced by magnetron [17], [18]. The so-called Haberland type GAS was further simplified at our department [14], [19]–[21] and its efficiency has been considerably improved. Other types of

GAS have been developed based on the laser evaporation [22], or the arc evaporation [23], but their application is hindered by the price of the sources and other problems.

In this work we will discuss specifically the magnetron-based gas aggregation source. Compared to the original Haberland source [17], [18], it has only one orifice (aggregation chamber leads directly to the deposition chamber) to maximize nanoparticle extraction and it is cooled only with water (not by liquid nitrogen). It uses a magnetron either for sputtering of the material for NPs formation [14], [15], [24]–[26] or for the plasma-activation and polymerization of gaseous precursor introduced into the aggregation chamber [27]–[29]. With current technology it is not possible to produce NPs in such high quantities as using chemical methods, but the NPs may be produced in highly clean environment without use of toxic substances or surfactants needed to keep the NPs suspended in liquid. On the other hand, direct deposition on any vacuum compatible substrate is relatively simple and without the solution there is almost no aggregation of the NPs on substrate. The typical design of such source is shown in Figure 1.

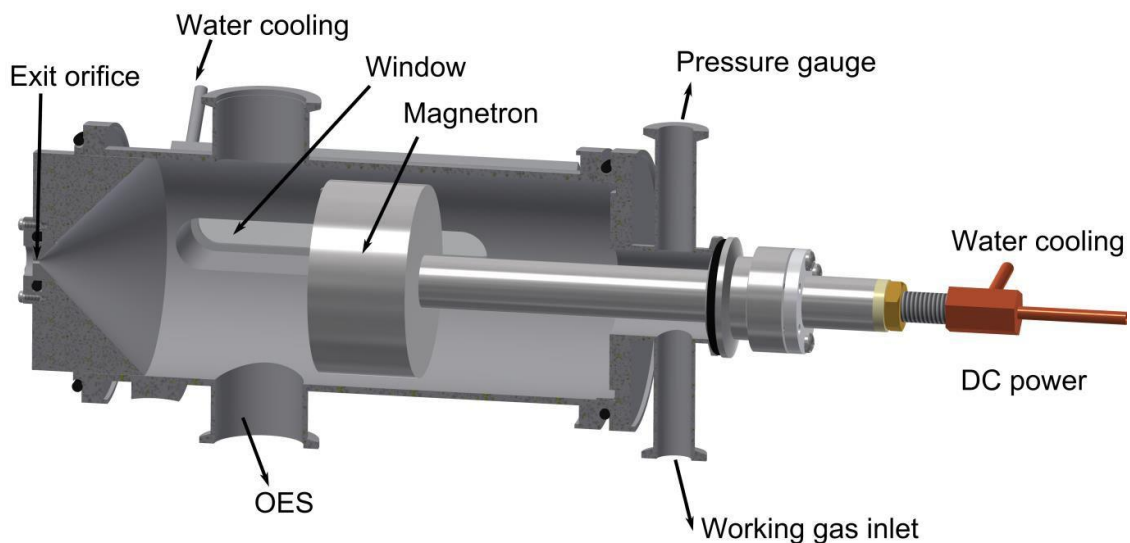


Figure 1: Example of magnetron-based gas aggregation source used in our group. Reproduced from [PS 1].

This design uses a magnetron inserted into a cylindrical aggregation chamber terminated by a conical lid with replaceable exit orifice leading into the main deposition chamber where the substrate is placed. The magnetron was always cooled with water. The walls of the aggregation chamber were cooled with water when depositing metal NPs, because it was crucial for the stability of the NPs formation process. In case of the pure plasma polymer or the plasma polymer containing NPs, the cooling of the walls was found to have little or no effect.

The magnetron-based gas aggregation source may be used in multiple ways to produce NPs. The simplest one is the DC sputtering of a metal target in an inert gas [14], [20], [21], [30]–[32]. This is probably the most common method of the production of metal NPs. Similar results may be reached using the RF power, but due to potential problems with implementation of RF, it is usually not the preferred way for metal NPs production. By injecting reactive gas to the aggregation chamber, the process may be changed to reactive sputtering. Depending on the concentration of the reactive gas, the resulting NPs may range from almost pure metal (the reactive gas is used in very low concentrations only to boost up the nucleation process) [30],[33] to fully metal oxide NPs [34]. Non-metal targets, such as ceramic [34] or polymeric targets [24], [35], [36], may be used in an RF discharge to produce metal oxide or plasma polymer NPs. Another possibility is the injection of an organic gas [27], [29], [37], [38]. If the organic gas is used with a polymer or carbon target, the plasma polymer NPs may be obtained similarly to RF sputtering of a polymer target. If the organic vapors are used with metal target, composite NPs may be formed [PS 4].

This type of source with various modifications has been used to deposit and investigate many different types of NPs including simple metal ones, plasma polymer NPs from both sputtered target and from gaseous precursor and composite NPs from either two metals or from a combination of metal and plasma polymer. These experiments will be described in the following chapters.

3 Composite nanoparticles

This chapter is devoted to the description of experiments with deposition of the composite NPs. Three systems have been investigated: copper-tungsten composite NPs from single copper target set with tungsten pellets, nickel-titanium composite NPs from two magnetrons in the same arrow-shaped deposition chamber and silver/hexamethyldisiloxane (HMDSO) plasma polymer NPs originating from sputtering of silver target in a mixture of argon and HMDSO.

3.1 CuW composite nanoparticles from a single target

The first discussed system includes the Cu/W NPs which were described in [PS 1] and [PS 2]. The motivation of this research was the creation of core-shell NPs in a very simple way. Instead of the separation of the core and shell deposition processes used e.g. in [39], we decided to do

everything in one step. To do so, it was necessary to choose a combination of immiscible materials. We chose a combination of copper and tungsten because we already had experience with the use of copper [40], and tungsten had also been previously used to make NPs in a gas aggregation source [41]. It is well known that copper and tungsten do not form true alloys and do not mix [42], even though some alloy-like materials are commonly used.

We have used two composite targets based on copper plate – one with 16 tungsten pellets in the erosion track, the other with maximum possible number of 37 tungsten pellets. The experiments were successful, and we were able to produce (especially with the 37 pellets target) core-shell NPs with tungsten core and copper shell. The core-shell character was proved both by a combination of EDX and XPS measurements and by TEM, see Figure 2.

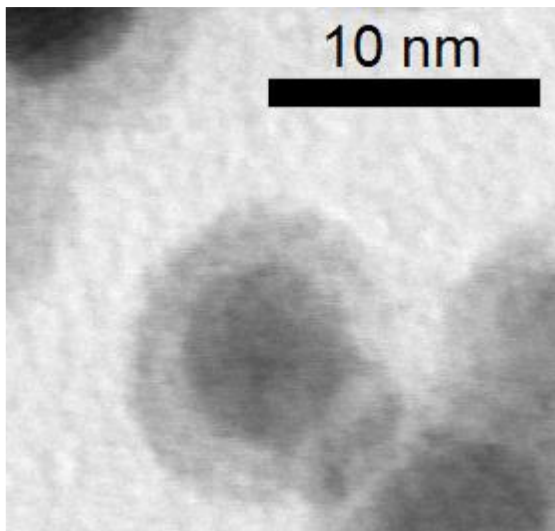


Figure 2: HR-TEM image of a core-shell nanoparticle containing 40% of tungsten prepared from target with 37 pellets. Reproduced from [PS 1].

We have, however, also observed some unusual effects. In continuous discharge, the deposition rate of the composite NPs was much lower than deposition rate of NPs produced from each single metal, see Figure 3. Furthermore, we have noticed that while the deposition rate with composite targets was low when plasma was on, there was always a flash of high deposition rate every time the discharge was turned off, see Figure 4. This means that the NPs had to be trapped inside the GAS when the plasma was on. Based on these observations we later attempted to study the NPs formation process directly using a small angle X-Ray scattering of synchrotron radiation [43], [44] where the trapping was directly observed.

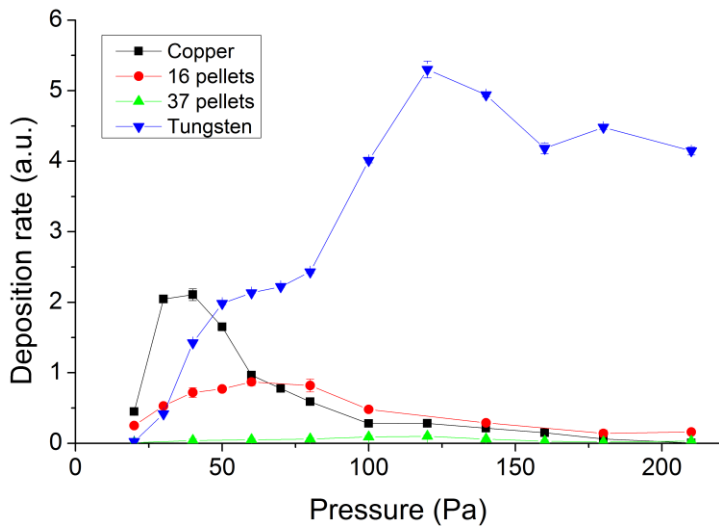


Figure 3: Deposition rates of NPs from four different targets: copper, copper with 16 pellets of tungsten, copper with 37 pellets of tungsten and tungsten

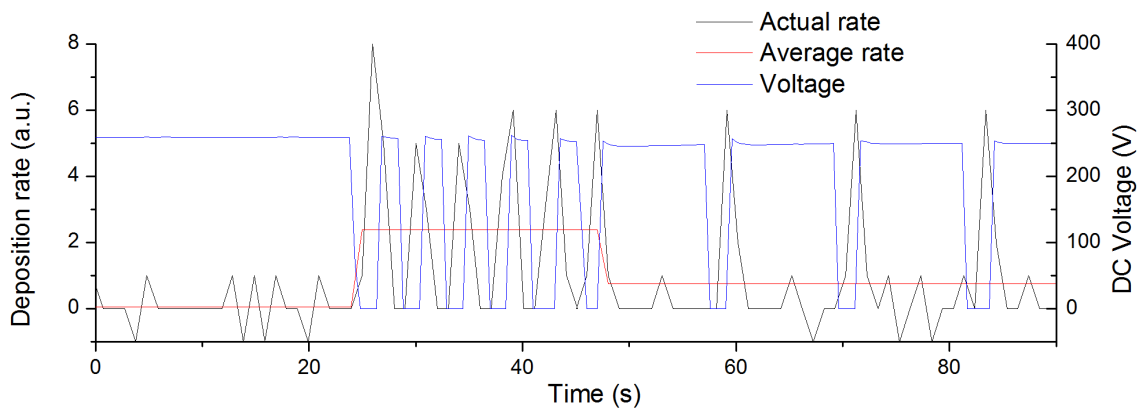


Figure 4: Dependence of the deposition rate on the pulsing of the discharge (37 pellets, pressure 180 Pa, magnetron current 500 mA). Subsequent examples of the instantaneous deposition rate (1s sampling) in continuous mode, pulsing mode with 2s on/2s off and with 10s on/2s off time.

The observations shown in Figure 3 and Figure 4 have not yet been published elsewhere, because we are not yet able to properly explain the mechanism why the composite NPs should be trapped so much more than the single metal ones. The answer is most likely in the material constants [45] and their shift with the interaction of copper and tungsten, but proper explanation does not yet exist because of the high complexity of both the trapping mechanism and the charging mechanism of NPs, especially the composite ones.

In order to understand the formation of the composite NPs, we have invited colleagues from Kiel who brought a calorimetric probe to investigate energy flux inside the aggregation chamber in our setup using plain copper, plain tungsten and composite Cu/W target with 37 pellets of

tungsten in the erosion track. While the results of the work described in [PS 2] by themselves are not sufficient to understand the growth and trapping mechanisms, they contribute to the overall picture.

The passive thermal probe (PTP) is schematically shown in Figure 5. It consists of a small copper platelet with thermocouple and biasing wire spot-welded from behind and set into a shielding tube to ensure that the signal is measured only from the front side. The main function of the probe is to measure energy flux from changes of its temperature, but it may also be used as a planar Langmuir probe to help with energy flux analysis. There are multiple methods to conduct the measurement, but since the magnetron power source may be easily switched on and off, the method using so called heating and cooling kinks was chosen. The kink is the change of temperature derivative when the plasma is switched on or off. From these data we were able to deduce the energy flux as explained in detail in [PS 2].

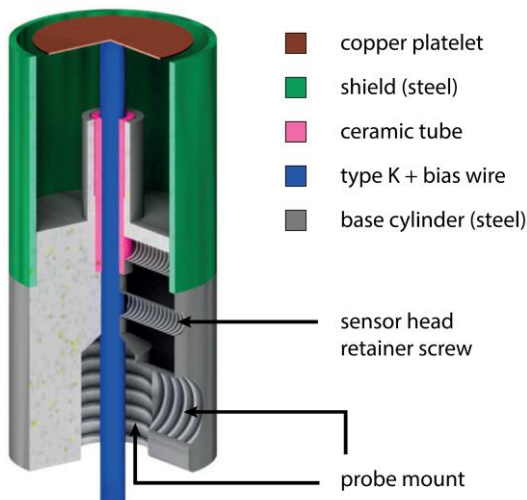


Figure 5: Schematics of the calorimetric passive thermal probe. Reproduced from [PS 2].

Aside from the energy flux, we measured the deposition rate and magnetron power (at constant current mode). The full set of measurements inside the aggregation chamber for the dependences on distance from the magnetron, magnetron current and aggregation chamber pressure are shown in Figure 6.

There are two main observations. In terms of magnetron power, the composite target behaves very similarly to the pure copper one, while in terms of energy flux, it matches the tungsten target. The explanation of both observations lies in the momentum transfer between copper, tungsten and argon. In the conditions of several tens of pascals, the mean free path of molecules is in submillimeter range. The sputtered atoms transfer their kinetic energy to the

argon gas that is being heated up as a result. This creates a region above the target with apparent pressure reduction in an effect called “gas rarefaction”. In this region the mean free path is longer and allows the energetic species to reach farther from the magnetron. Also, the impedance of the plasma in this region is higher which results in higher magnetron voltage. Since the copper has the mass much closer to argon than the tungsten it is a more efficient agent of the rarefaction causing the similarity between copper and composite target in terms of magnetron power. Even the amount of copper released from the composite target is evidently sufficient to achieve almost the same effect as with the pure copper target.

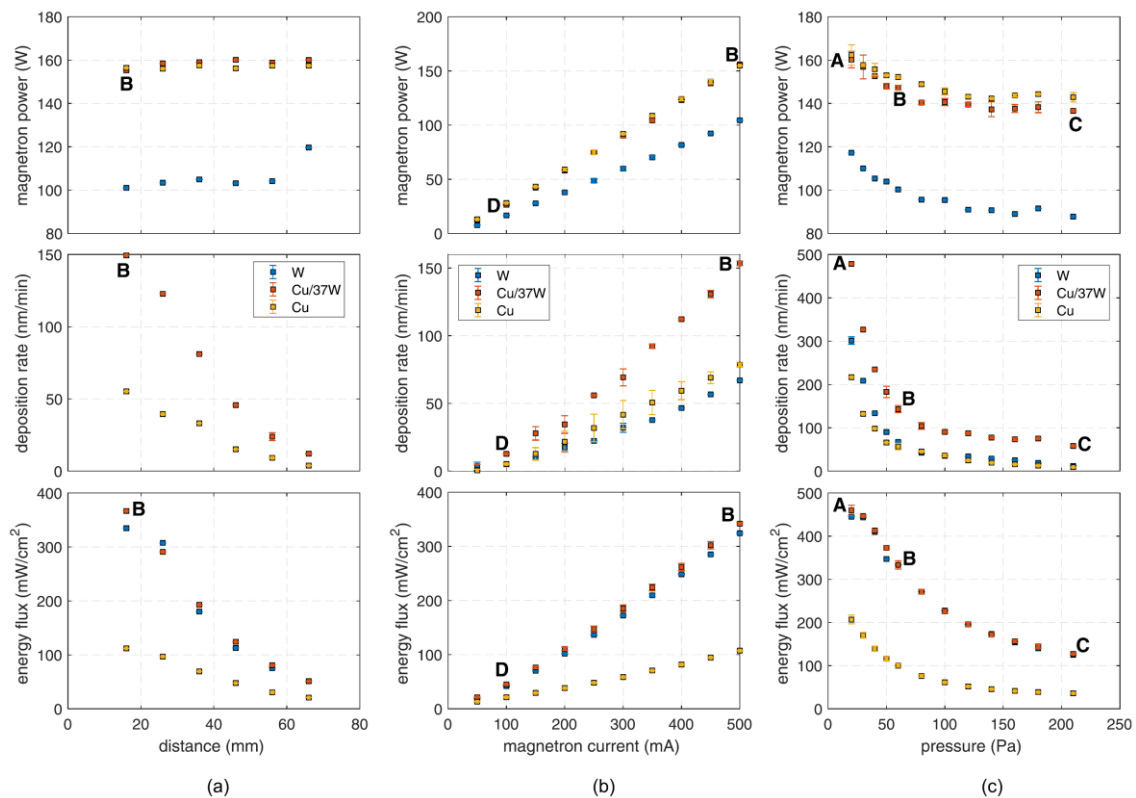


Figure 6: Summary of the magnetron powers, deposition rates and energy fluxes obtained for the investigated targets and parameter variations. (a) Variation of distance between probe and target with 500mA current and 60 Pa. Unfortunately, no distance variation has been performed while measuring the deposition rate for tungsten. (b) Variation of magnetron discharge current at 60 Pa and 16mm distance; (c) variation of gas pressure in the aggregation chamber with 500mA current at 16 mm distance. The bold letters A, B, C, D mark the data points for the corresponding SEM images presented in [PS 2]. Reproduced from [PS 2].

As for the energy flux, it was deduced from the Langmuir probe that the contributions from electrons, ions and plasma radiation are just a small portion of the total flux. Therefore, the main contribution must come from the sputtered atoms, reflected gas atoms, conduction from the heated gas and condensation heat. While the rarefaction is stronger for the copper and allows longer mean free path of the molecules, there is even greater difference between the amount

of argon atoms reflected from the target upon impact. It is expected that about 1% is reflected in case of copper, while about 10% of the argon atoms are reflected from tungsten. This seems to be the main factor driving the similarity between composite and tungsten target in terms of energy flux.

A correction on the same input power should be made to properly compare energy flux between targets. This was done using a simple relation:

$$\eta = \frac{J_s}{P_{mag}/A_{mag}} \quad (1)$$

where J_s is the energy flux, P_{mag} is the magnetron power and A_{mag} is the area of magnetron surface. The normalized plots of the energy flux are presented on Figure 7. It shows that the shape of the dependences for the composite target is still driven by tungsten, but required normalized power now lies between copper and tungsten, as would be expected.

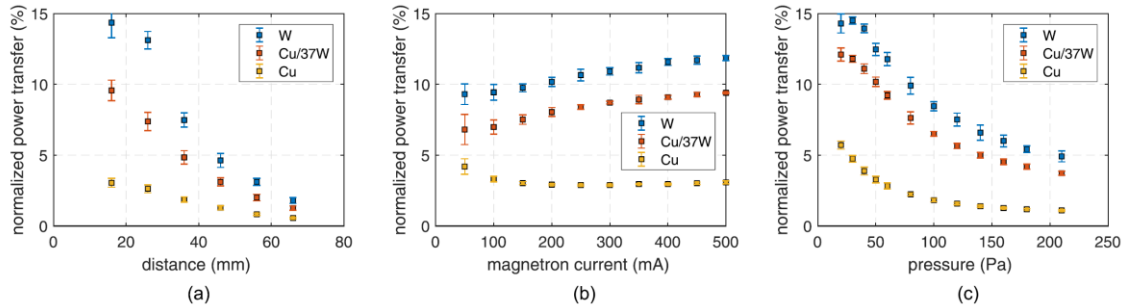


Figure 7: Summary of the PTP results normalized with the magnetron power according to equation (1). (a) Variation of the distance between the probe and the target with current 500mA and pressure 60 Pa, (b) variation of the magnetron discharge current at pressure 60 Pa and distance 16mm, and (c) variation of the gas pressure with current 500mA current at distance 16 mm. Reproduced from [PS 2].

3.2 Titanium/nickel composite NPs from two magnetrons in the same aggregation chamber

While the use of a single segmental or composite target is very convenient and effective in some cases and for specific combinations of materials, it is not universally applicable. It has its intrinsic limitations such as that only some combinations of materials may be used or the fact that the composition of the NPs is mostly given by the composition of target with little space for variation. We have tried to eliminate these limitations by using of two magnetrons in one aggregation chamber [PS 3]. This approach differs significantly from the sequential deposition in e.g. [46]–[50] because in our case, both magnetrons are in the same deposition chamber. Because there is no orifice and therefore no acceleration of the NPs between the magnetrons, the NPs move slowly, and have much more time to collect the material and form a shell. To avoid

potential problems with uniformity of the NPs (formation of NPs with excess of one material in the vicinity of its respective target), the magnetrons were not placed side by side as e.g. in [51], [52], but perpendicular to each other in an arrow shaped aggregation chamber, see Figure 8.

The idea was that NPs would nucleate in the vicinity of the retracted magnetron (on the right), move along the aggregation chamber past the second magnetron (left) where they meet vapor of the second material to form the shell around the already fabricated cores. This experiment was carried out with nickel on the first (retracted right-side magnetron) and titanium on the second (inserted left-side) magnetron and Ni@Ti core-shell NPs were successfully deposited. Aside from the simple deposition, we have investigated the influence of the deposition conditions on the presence and amount of single metal NPs. We used EDX mapping to investigate which NPs are core-shell and which are only single metal ones as well as what is the size of the core and thickness of the shell.

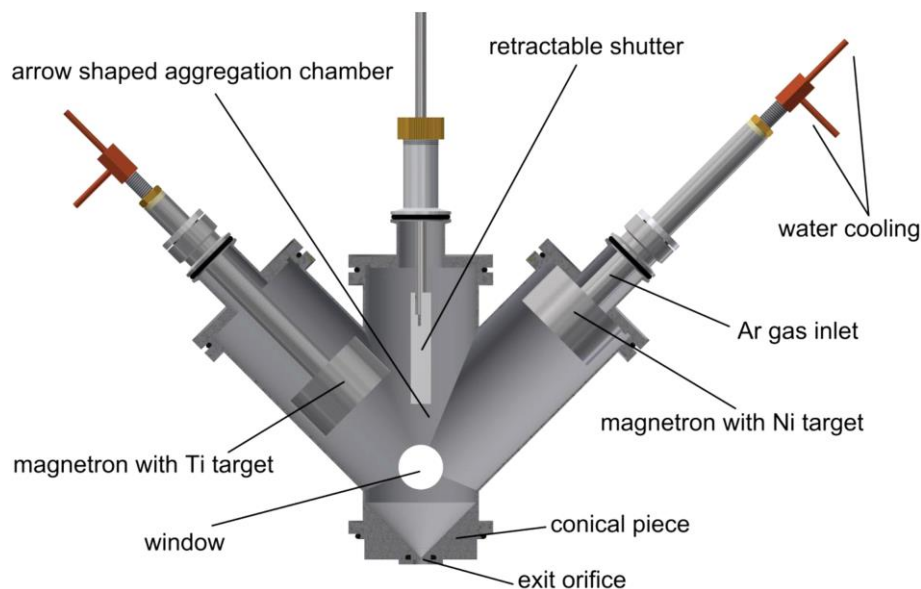


Figure 8: Schematics of arrow shaped GAS for production of NiTi NPs. Reproduced from [PS 3].

The magnetron current on the first magnetron with nickel target was set to 400 mA, the current on the other magnetron with titanium was varied between 0 and 600 mA. The results are presented in Figure 9. It may be seen in Figure 9a that with no discharge on titanium magnetron, we of course produced only nickel cores. At 200 mA we obtained about 60% of core-shell NPs, but the amount of titanium was evidently not sufficient to cover all NPs. The best results were achieved with 300 mA where almost all of the NPs were core-shell. At even higher current, the concentration of titanium was high enough to spark nucleation of a small portion of pure titanium NPs.

Another important effect is shown in Figure 9b. As the power to the second magnetron with titanium target increased, the size of the nickel NPs/cores decreased. Since the two magnetrons were separated with enough distance not to interfere with each other, we assume that the nickel NPs size was the same at the beginning, but as they passed through the discharge area of the titanium magnetron, they began to evaporate and shrink. We can even see that as the magnetron current increased, even the shell was decreasing in thickness due to the competition between deposition and evaporation. Evaporated nickel atoms may have actually served as seeds for nucleation of titanium NPs observable at higher currents.

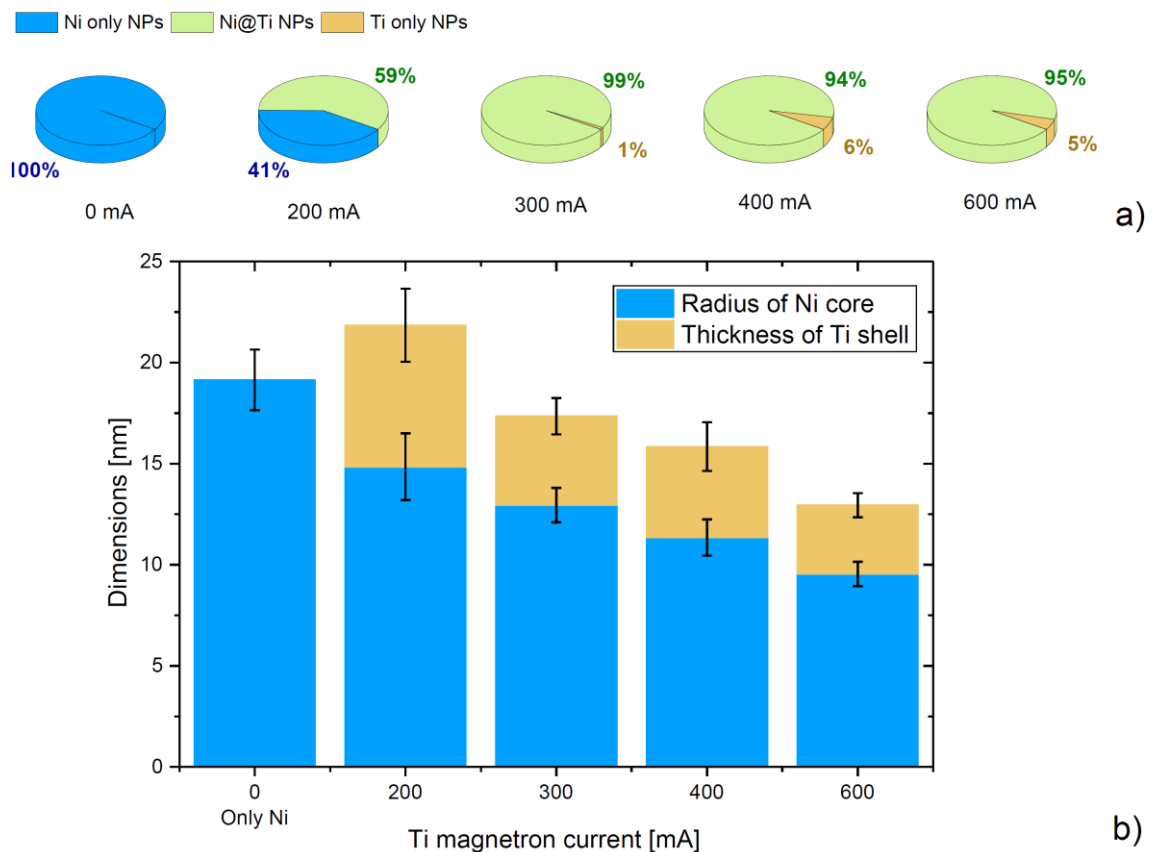


Figure 9: (a) Portion of the Ni, Ti and Ni@Ti NPs produced at different Ti magnetron currents and (b) the sizes of Ni cores and Ti shells as obtained from EDX STEM maps. Each core/shell has been fitted with a circle, whose diameter has been used in statistics. Reproduced from [PS 3].

3.3 Composite metal/plasma polymer NPs

I conducted the work presented in this chapter in Kiel as part of the group led by prof. Franz Faupel. The goal was to prepare composite core-shell NPs with metal core and plasma polymer shell. For this purpose, a high-flow rate GAS with 2-inch magnetron was used. Silver was selected as the metal, while HMDSO was used as a precursor for the plasma polymer shell. While HMDSO

is a common precursor for the plasma polymerization, it is also capable of producing SiO₂ when mixed with sufficient amount of oxygen.

The magnetron was mounted with silver target and was originally operated in DC mode to test the production of silver NPs. Then, still in the DC mode we have introduced the HMDSO monomer and obtained NPs that contained carbon and silicon, but according to TEM measurements, the NPs did not seem to have a core-shell character. Therefore, we have switched to RF. Although with RF, it was impossible to produce pure silver NPs (in the current setup), this system was highly efficient in the production of composite core-shell NPs. We believe that the RF is more efficient because, compared to the DC, the processes relevant for the plasma polymerization are pushed more into the plasma volume. Even though the amount of sputtered metal is probably lower and insufficient for effective nucleation by itself, with the help of the monomer, it is possible to successfully form the core shell NPs (see Figure 10). The ratio between metal and plasma polymer may be controlled by the amount of injected monomer.

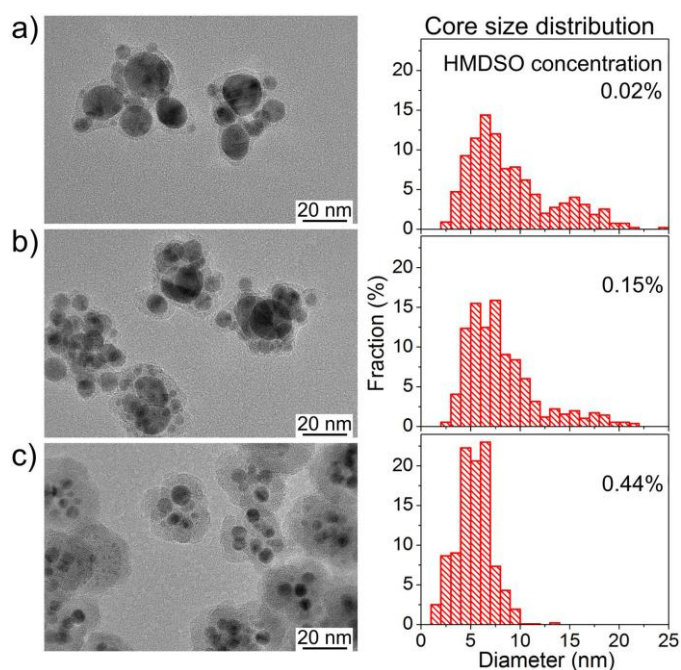


Figure 10: TEM images and the core size distributions of the multicore-shell NPs prepared by GAS at different concentrations of HMDSO: (a) 0.02%, (b) 0.15%, (c) 0.44%. Reproduced from [PS 4].

Even though it was not possible to produce pure silver NPs in RF, we have instead managed to generate pure plasma polymer NPs (without metal). This was achieved by replacing the silver target with the carbon one. We were also able to prepare core-shell NPs with the matrix composed of SiO₂ rather than the plasma polymer which was achieved simply by the addition of

oxygen into the gas mixture, see Figure 11. Using XPS and FTIR it was determined that the shell is indeed almost stoichiometric SiO_2 with only faint traces of carbon.

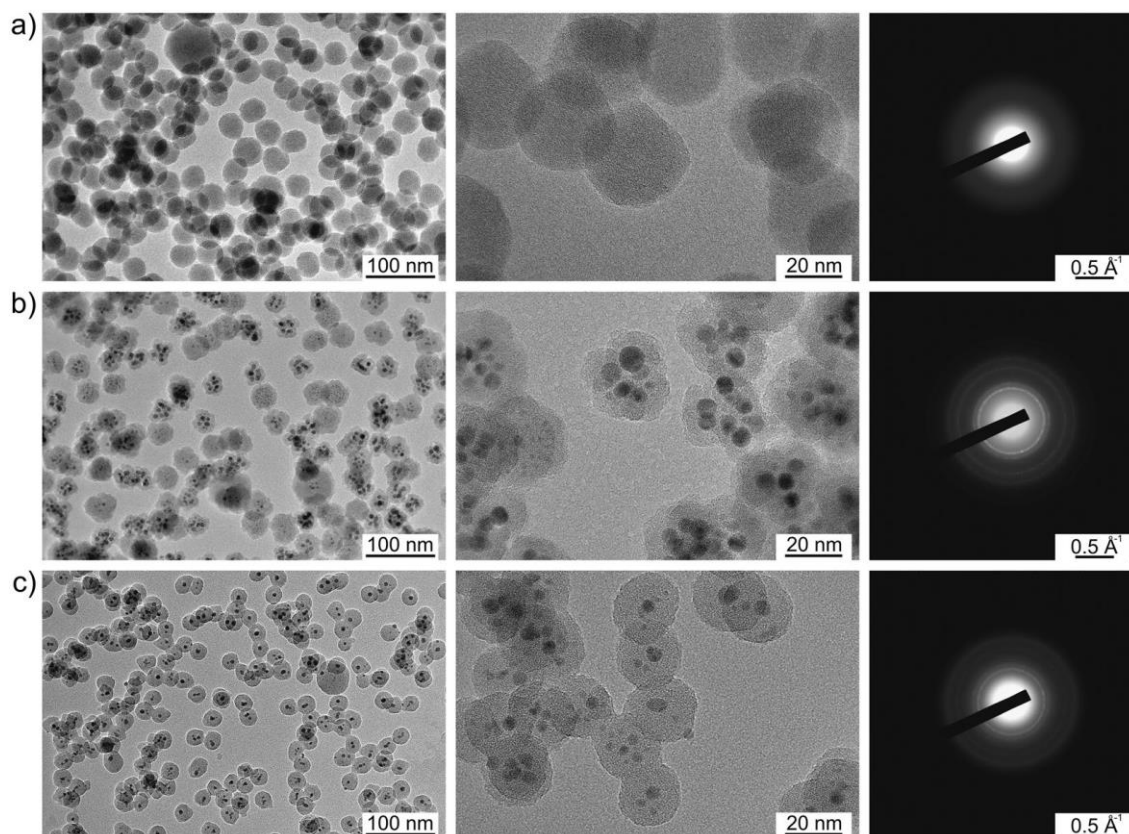


Figure 11: TEM images with lower (left column) and higher (middle column) magnification of the NPs prepared by GAS: (a) from the Ar/HMDSO mixture with graphite target and (b) from the Ar/HMDSO mixture with Ag target (in both cases the HMDSO flow rate is 0.45 sccm); (c) from the Ar/HMDSO/O₂ mixture with Ag target (0.15% HMDSO, 3.8% O₂, Ar flow rate 105sccm, pressure 190 Pa). The right column shows the corresponding diffraction patterns. Reproduced from [PS 4].

Since the Ag/plasma polymer or Ag/SiO₂ composite NPs are metal inclusions in transparent matrix, they evince anomalous absorption from localized surface plasmon resonance (LSPR). Depending on the inclusions size and matrix composition, it is possible to tune the absorption band. The example of the dependence of the absorption on the HMDSO concentration is shown in Figure 12. At the low concentration of HMDSO, there is a bimodal size distribution of the metal cores causing wide LSPR absorption band composed from two shoulders. As the concentration of HMDSO increases the band becomes narrower and at highest concentration there is just a narrow band originating from narrow size distribution of the NPs cores.

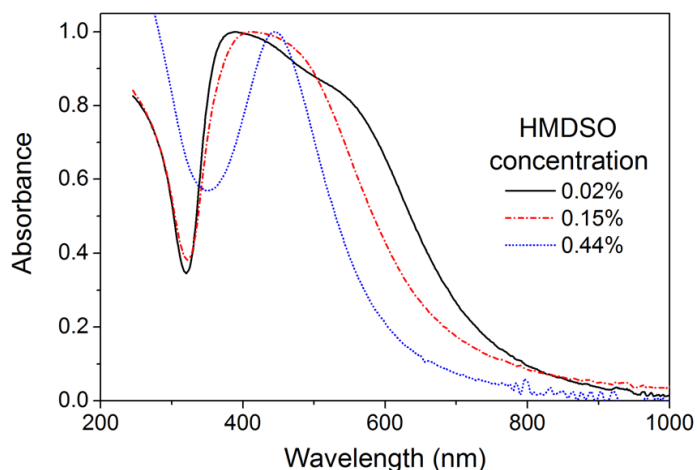


Figure 12: UV-Vis spectra of the core-shell nanoparticles prepared by GAS at different concentrations of HMDSO. Reproduced from [PS 4].

4 Measurement of nanoparticles speed

In our early experiments with plasma polymer NPs [24], [27]–[29], [36], [53], we have observed deposition discrepancies. These included unusual shapes of the deposits (e.g., with the lowest deposition in the center of the nanoparticle beam) or anomalous dependency of the deposition rate on pressure in the deposition chamber (the increase of background pressure should scatter the NPs and cause monotonous decrease of deposition rate with increasing pressure, but instead a peak function was observed). Originally, we attributed these effects to aerodynamic focusing of the nanoparticle beam. However, the careful comparison to the gas flow simulation revealed it to be impossible. Furthermore, the comparison with theoretical models suggested a relation of deposition rate to the NPs speed. That sparked the idea, that most of the observed phenomena may be ascribed to NPs reflecting from the substrate when they hit it too fast (the description of these effects is presented in chapter 5). However, there was no way to directly prove it. This led to the effort to develop a suitable method for the measurement of NPs speeds. Many methods were rejected because of too complicated measurement or analysis [15], limitations on the size of the NPs [54], [55] or the reliance on charged NPs only [56]. We have chosen a method originally developed for energy filtration of neutrons or molecular beams [57]–[62] – slotted disks speed selector – and modified it for purposes of measurement of NPs speeds. This tool, as well as the measurement of the NPs speeds with it is described in the following text and in publications [PS 5] and [PS 6]. It was first tested on copper NPs because of the considerably easier measurement compared to plasma polymer NPs.

4.1 Description of mechanical time-of-flight filter

At first, we started with a simple setup with two slotted disks (Figure 13a) and studied the resolution and throughput of the device. Later we moved to the more complicated helical rotor (Figure 13b) that allows much higher throughput of NPs with much lower losses and therefore stronger signal. The basic idea of both filter types is the same. The main difference lies in the fact that the helical rotor has isolated channels that prevent the nanoparticles to exit through other than intended slit, allowing to place the channels much closer to each other, see Figure 13c,d. The nanoparticle enters one of the rotor channels and if its speed corresponds to rotor geometry and rotation rate, it exits on the other side. If it does not fly through, it is either deposited inside the rotor or it is reflected away from the direction of the nanoparticle beam.

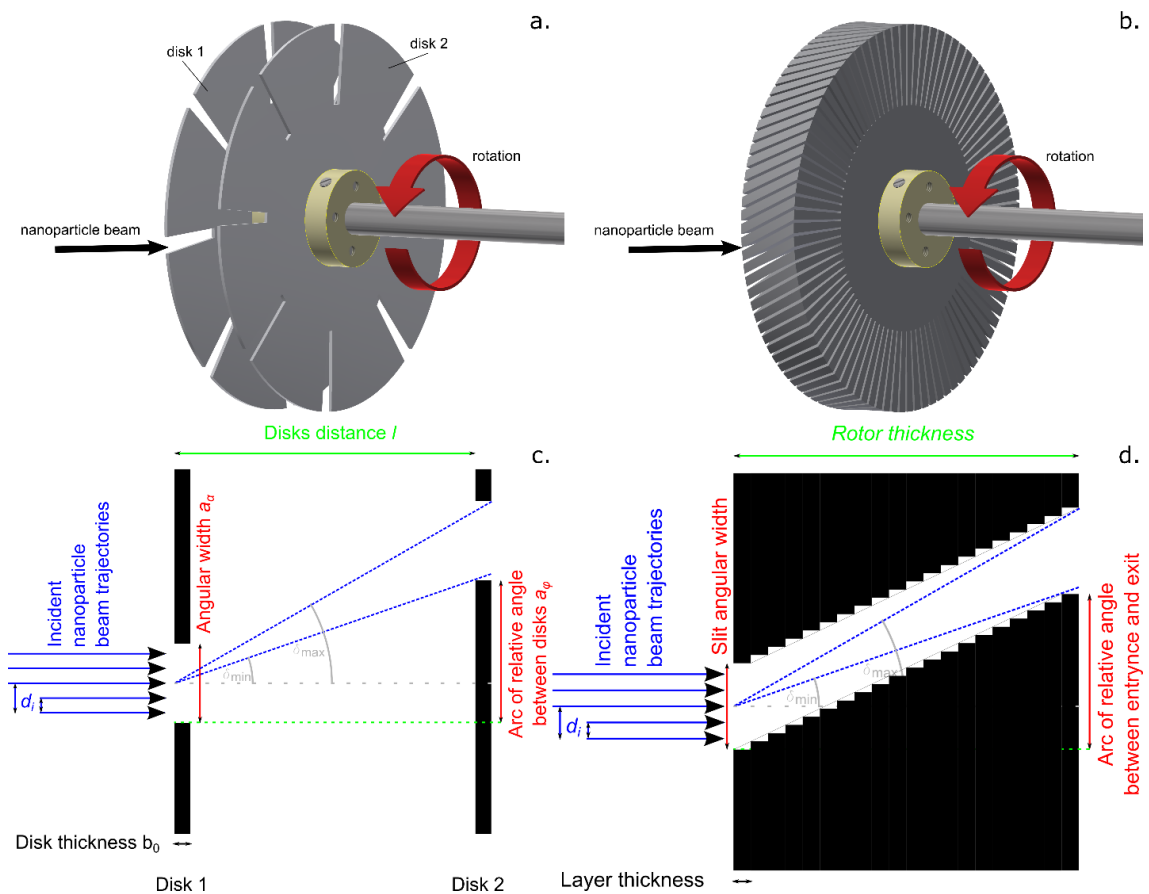


Figure 13: Schematics of the nanoparticle time-of-flight filter rotors: (a) slotted disks with 8 slits of angular width 5° on each disk. The relative angle between the disks is 9° , disk-to-disk distance is 19 mm, disk thickness is 1 mm; (b) helical rotor with 90 slits of angular width 1° , the relative angle between entrance and exit 9° , total thickness 20 mm and printing resolution 0.2 mm; (c) schematic illustration of the model of the slotted disks; (d) schematic illustration of the model of the helical rotor. Reproduced from [PS 5].

The rotors in this work were 3D printed from PETG polymer that has very convenient mechanical properties for this purpose. While the slotted disks may be manufactured in the

traditional way (even though much more expensive), the helical rotor has too complicated shape for the traditional machining. It is basically composed of layers of thin slotted disks, each rotated by an incremental angle. That is very easy job for the 3D printer (it is exactly how the 3D printer works). On the other hand, it would be almost impossible to make it by milling from solid block (at least in the case of high-resolution rotors with narrow slits). These layers are shown in Figure 13d as steps in between the entrance and exit.

Based on the previous works [59], [61], we assembled a mathematical model of the rotor – its instrumental function – necessary for the proper analysis of the measured signal. Any measurement is always a convolution of the real speed distribution and the instrumental function of the rotor. Narrower slits mean less distortion of the signal and in the limit of infinitely narrow slit there would be just the real speed distribution. We used the known instrumental function to deconvolute the measured signal to obtain the speed spectra of the NPs. In order to make the fit, a fitting software had to be created since the process was too complicated to be carried out in e.g. Origin software.

The instrumental function may be deduced from the basic parameters of the rotor geometry, and it is the same for both the slotted disks and the helical rotor. The important parameters for the calculation are the distance between the disks (rotor thickness), the relative angle between the entrance and the exit slit, the angular width of the slits, and the thickness of the disks (in the case of slotted disks) or the layer thickness (in the case of the 3D printed helical rotor), see Figure 13c,d. From these parameters, it is possible to determine the shape of the instrumental function based solely on the geometry. The detailed description of the calculation is available in [PS 5]. The example of the instrumental function for 4 different rotors is shown in Figure 14.

As would be intuitively expected, the instrumental function narrows down for narrower slits. The difference between the slotted disks and the helical rotor, both with the same slit width, total thickness and angle between entrance and exit, lies in the difference between the disk/layer thickness. While disks were 1 mm thick, the layer thickness of the 3D printed helical rotor was only 0.2 mm, therefore, the helical rotor provided higher throughput. On the contrary, when discs were used, part of the beam was shadowed by the upper part of the entrance slit and the edge of the exit slit (see Figure 13c,d).

The maps presented in Figure 14 may be interpreted in two important ways. Every horizontal cut represents the signal distortion by the instrumental function for the specific single

NPs speed. On the other hand, each vertical cut shows the spectrum of NPs speeds that are transmitted at the specific rotor rotation rate.

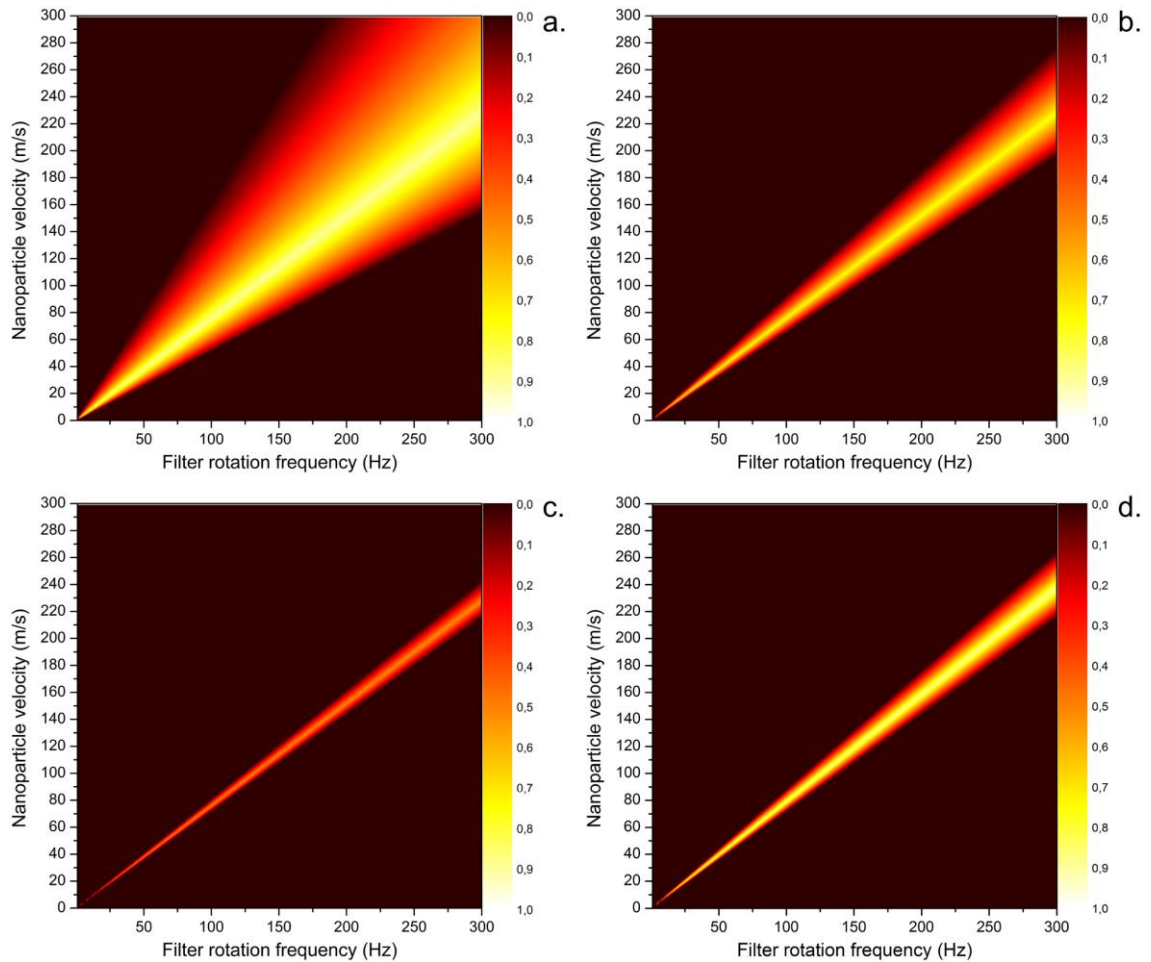


Figure 14: Calculated transmission signal maps for input nanoparticle velocities in the form of delta-functions, the relative angle of the disks 9° , the distance of the disks 19 mm, the disk thickness 1 mm and the angular width of the slit (a) 5° ; (b) 2° ; (c) 1° . The last map (d) shows the transmission of a helical rotor with a relative angle of the slit between the inlet and outlet of the slit again 9° , slit angular width 1° and thickness of the rotor 20 mm. The print resolution for the helical rotor (thickness of each subsequent incremental disk) is 0.2 mm. Reproduced from [PS 5].

In any real experiment, there is never just a single nanoparticle speed. As will be discussed further, the speed is size-dependent, but even if all the NPs were the same, the interaction of the NPs with the gas in the orifice would lead to establishment of a Gaussian distribution of speed along the beam axis. That means the measured spectrum is a superposition of different speeds, each interacting with a different part of the instrumental function. As mentioned above, a convolution of the instrumental function and the real speed distribution produces the measured signal in terms of deposition rate vs. rotor frequency. The example is shown in Figure 15. Details on how to make the convolution may be found in [PS 5].

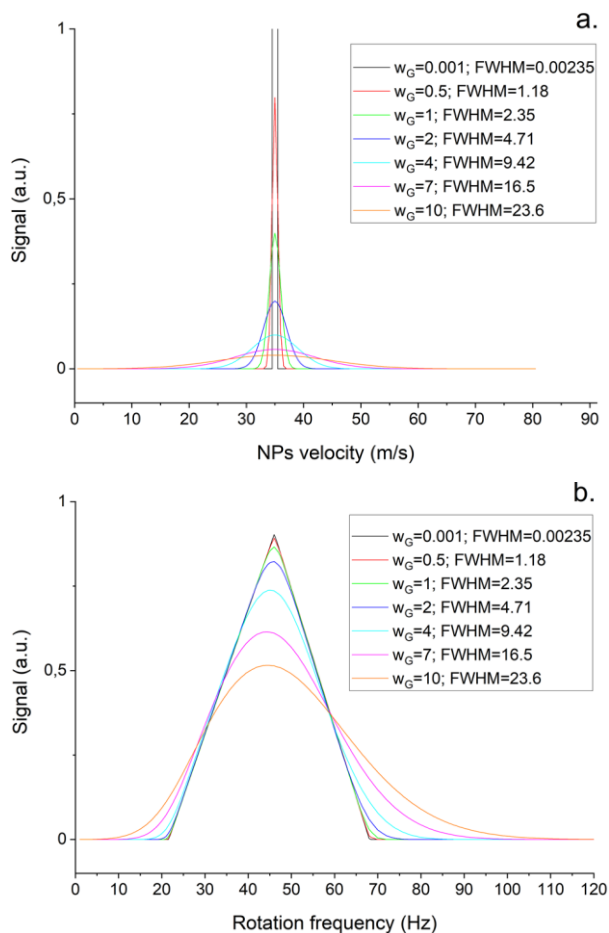


Figure 15: (a) Gaussian velocity distributions; (b) Simulation of the signals obtained from 5° disks for Gaussian velocity distributions. Reproduced from [PS 5].

4.2 Processing and deconvolution of measured data

Since a direct deconvolution of the measured signal is very complicated, the inverse approach was implemented. Instead of deconvoluting the measured signal, we started with a seed function, convoluted it with known instrumental function and compared the result with measured data. Then the seed function was modified, and the process was repeated until the best fit with the measured data was reached. The quality of the fit was evaluated by the residual sum of squares (RSS).

Two approaches were used. The first one consisted of a simple fitting of the measured data with a single gaussian peak. It was the easiest first step and it also allowed us to quantify the speed distribution in simple terms of position of the maximum and the width of the distribution. This approach was first used in [PS 5] to measure the NPs speed at two different aggregation chamber pressures. The experiment was mostly designed to check that different rotors give the same deconvoluted speed distribution, which was confirmed (see Figure 16).

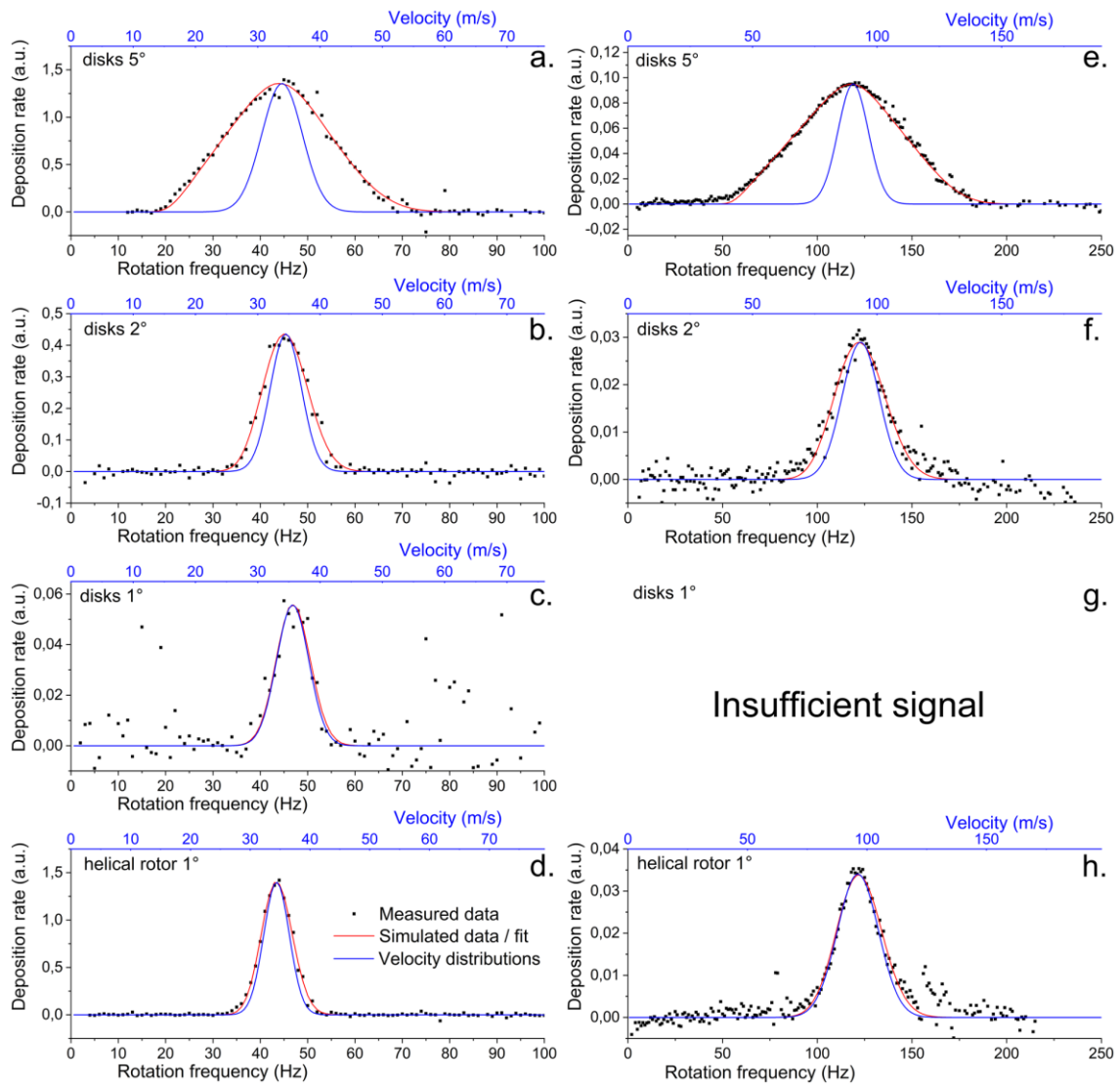


Figure 16: Comparison of the model with real measured data. Experimental deposition rates were obtained using a quartz crystal microbalance (QCM) sensor. (a–d) Nanoparticles deposited at aggregation chamber pressure 20 Pa, deposition chamber pressure 0.015 Pa, DC magnetron current 200 mA and QCM averaging over 5 values; (e–h) nanoparticles deposited at aggregation chamber pressure 100 Pa, deposition chamber pressure 0.15 Pa, DC magnetron current 200 mA and QCM averaging over 20 values. The relative angle of the inlet and exit slit was 9°, disk distance 19 mm, disk thickness 1 mm, thickness of helical rotor was 20 mm printed with layer thickness 0.2 mm and the angular width of the slits was (a,e) disks 5°; (b,f) disks 2°; (c,g) disks 1° and (d,h) helical rotor 1°. The lower black axis is the directly measured frequency of the rotor, the upper blue axis is formally converted to velocity. The fits of the measured data in red are accompanied by the derived NPs velocity distributions in blue. Reproduced from [PS 5].

It was however clear that this approach did not give the whole extent of the information stored in the measured data since there was evidence of finer structure especially in measurements with narrow rotor slits and therefore high resolution. The theoretical models [63], [64] predict different speeds for differently sized NPs and the size distribution of the NPs is often non-gaussian. As a result, the speed distribution also may be non-gaussian. Therefore, the first approach was expanded, and the fitting was done using a combination of multiple gaussian

peaks. The result is basically an approximation of the real speed distribution with the superposition of gaussian functions. That allowed us to obtain high resolution speed spectra and to subsequently compare them to the size spectra of the deposited NPs. This approach was first used in [PS 6]. It should also be noted that the electronics was improved to reduce the noise, the fitting software was improved to incorporate multipeak fitting and also its calculation efficiency was considerably increased. Since the helical rotor provides dramatically higher sensitivity than slotted disks, all the subsequent measurements were conducted with it. An example of the multipeak fit is shown in Figure 17. This fitting approach was then used to analyze the results at various deposition conditions and to experimentally investigate the relation between size distribution and speed distribution of the NPs. The results are described in the following chapter.

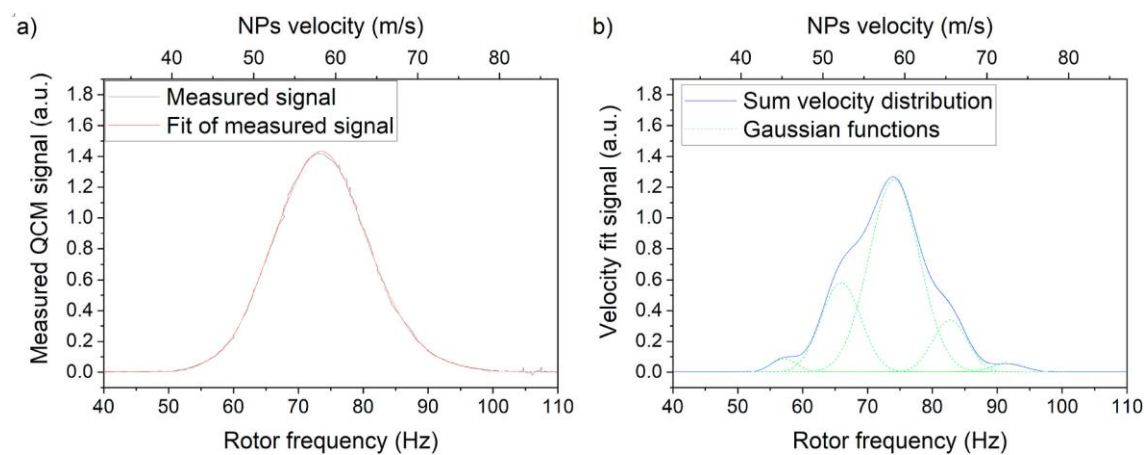


Figure 17: NPs velocity measurement for aggregation pressure 50 Pa and magnetron current 200 mA. a) measured QCM signal vs rotor frequency and its fit; b) NPs velocity distribution deconvoluted from the measurement. Reproduced from [PS 6].

4.3 Dependency of NPs speed on mass and aggregation chamber pressure

As predicted by the theoretical models [54], [63]–[65], there is a relationship between the NPs size and speed. The exact shape of the relation is dependent on many parameters and differs among the models. However, the models provided a hint of the basic shape of the relation function that may be used to fit the size distribution to the speed distribution. We determined the function to be used as

$$v = Ad^{-b} \quad (2)$$

where v is the nanoparticle speed, d is its diameter and A and b are fitting coefficients. Of these two, b represents the width of the speed distribution. Its value is highly dependent on the length of the orifice. The longer orifice pushes the b coefficient to lower values representing

narrower speed distribution. There are probably other parameters, that influence the value as well (albeit to a lesser extent), such as the morphology of the nanoparticle surface, but quantifying these is currently very difficult.

But even though the full extent of the influence of the deposition conditions and NPs properties is not yet known, the equation (2) has still very high value, because it allows us to separate the influence caused by the mass of the nanoparticles from other effects. After finding the coefficients by fitting of the mass spectra to the speed spectra, it is possible to easily calculate the speed of any nanoparticle size. That allows us to directly compare specific sizes between different deposition conditions even if the size distribution of the NPs shifts, for example, to compare NPs speeds at varying aggregation chamber pressure. Aggregation chamber pressure is arguably the most important parameter that influences the formation of the nanoparticles. It governs the sputtering efficiency, aggregation efficiency and also properties of the trapping region near the magnetron. Changing of the pressure therefore often leads to changes in the size distribution of the NPs. To study the influence of the aggregation chamber pressure on the NPs speed properly, it is necessary to separate the influence of the changing mean size. This was described in [PS 6] on the example of the copper NPs. First, it was shown how the equation (2) may be applied, see Figure 18.

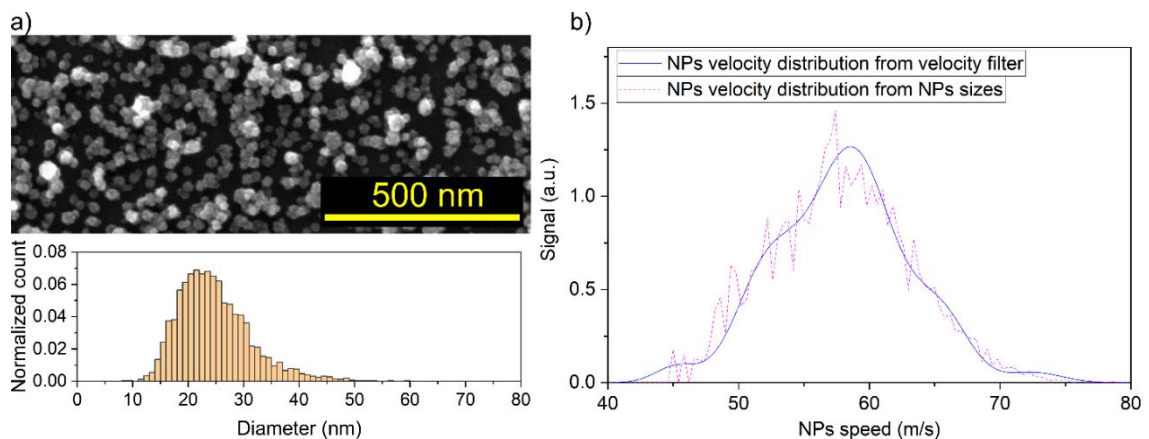


Figure 18: a) Scanning electron microscope (SEM) micrograph of Cu NPs prepared at aggregation chamber pressure 50 Pa and magnetron current 200 mA and their size histogram (total of 2512 nanoparticle sizes were used for the histogram in this case; normalized count means that the sum of all bars is 1). b) Comparison of the measured velocity distribution and velocity distribution determined from measured NPs sizes using equation (2). Reproduced from [PS 6].

Consequently, the method was applied to different pressures in the aggregation chamber. Figure 19 shows the dependency of the NPs speed on the aggregation chamber pressure both for the as measured mean speeds and the calculated speeds of NPs of specific sizes. The plot also shows that as the aggregation chamber pressure increases the speed distribution becomes

wider. However, this behavior can be expected because as the pressure grows, the speed of the gas and the NPs increases as well making place for bigger speed differences.

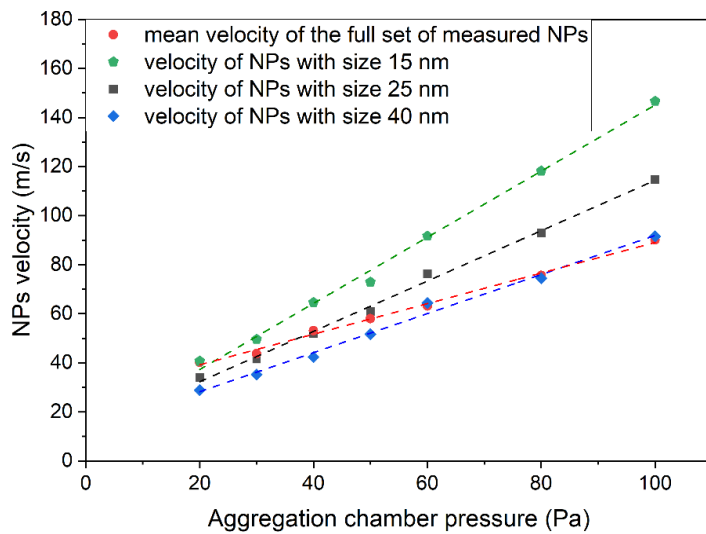


Figure 19: Measured dependency of NPs velocity on aggregation chamber pressure for three different nanoparticle sizes. Reproduced from [PS 6].

In some cases, we were able to obtain deposits with bimodal size distribution, see Figure 20. There were two types of NPs – the regular ones and the big aggregates that seemed to be composed of the regular sized NPs. The above-mentioned size-speed fitting was also successfully applied with a small modification. Since the aggregates were composed of small NPs, there had to be voids inside the big particles and therefore they had lower mass density than the regular nanoparticles. Therefore, the fitting had to be separated for regular NPs and aggregates and both had to be summed into the final fit. The result is shown in Figure 21. Because of the different mass density, the parameter A was different for the two peaks as the big NPs are accelerated to 1.37 times higher speed than would be expected for the NPs with the same size, but mass density same as the regular NPs.

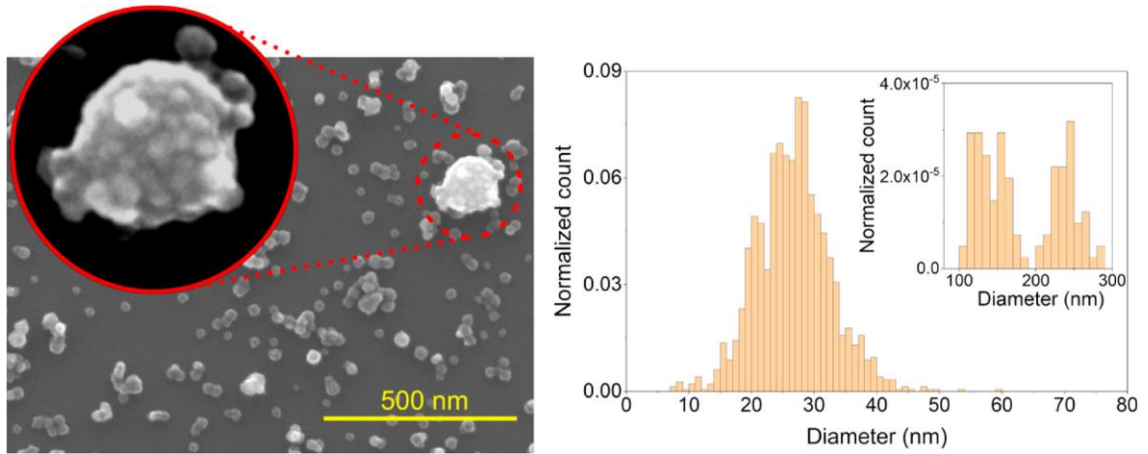


Figure 20: SEM micrograph of the NPs prepared at aggregation chamber pressure 50 Pa and magnetron current 100 mA with detail of one big nanoparticle composed of smaller ones and size histogram. The big particles are rare by number but are so big, that they carry notable mass and contribute to the QCM signal. Reproduced from [PS 6].

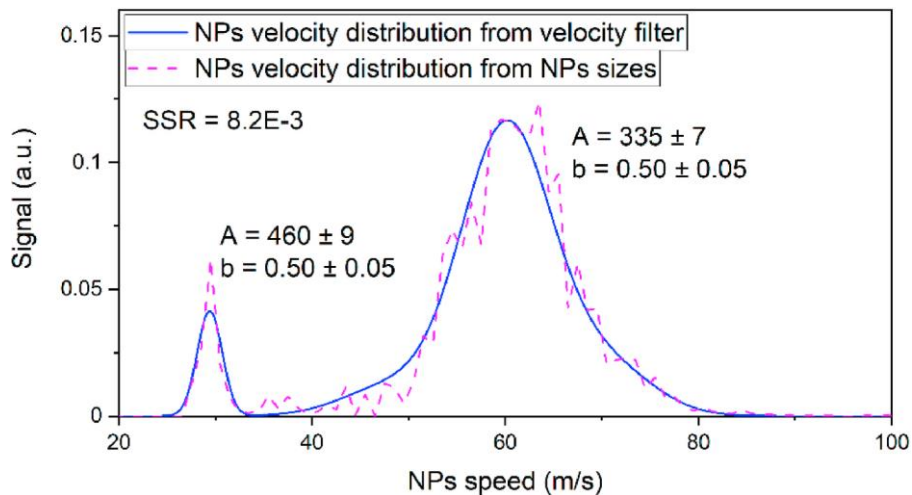


Figure 21: Comparison of the velocity distribution obtained from the velocity filter and from NPs sizes from SEM converted to velocity vs mass using equation (2). Total of 1576 NPs were used for the size/velocity histogram in this case. Reproduced from [PS 6].

Since it was shown that the NPs speed is dependent on their size (mass), it means that the mechanical time-of-flight filter that is basically a speed filter, may be also used as a mass filter that is independent of NPs charge. Such application was investigated in the case of NPs size distribution shown in Figure 20. The mass filtration was investigated in three places. With the reference to Figure 21: in the center of the main peak at 63 m/s (80 Hz), at high-speed tail at 71 m/s (90 Hz) and in the center of the secondary peak at 29 m/s (37 Hz). The results of filtrations at 63 and 71 m/s along with the superposed original and filtered size distributions are shown in Figure 22. For simplicity, the big NPs part is not shown in the histogram, since as expected, no

big NPs were found in the filtered beam. The filtered size distribution is only slightly wider than would be expected based on the rotor instrumental function and size-speed fit function. Some slight widening is expected, since as mentioned above, even single sized NPs must have speed distribution of non-zero width because of random interactions with the buffer gas.

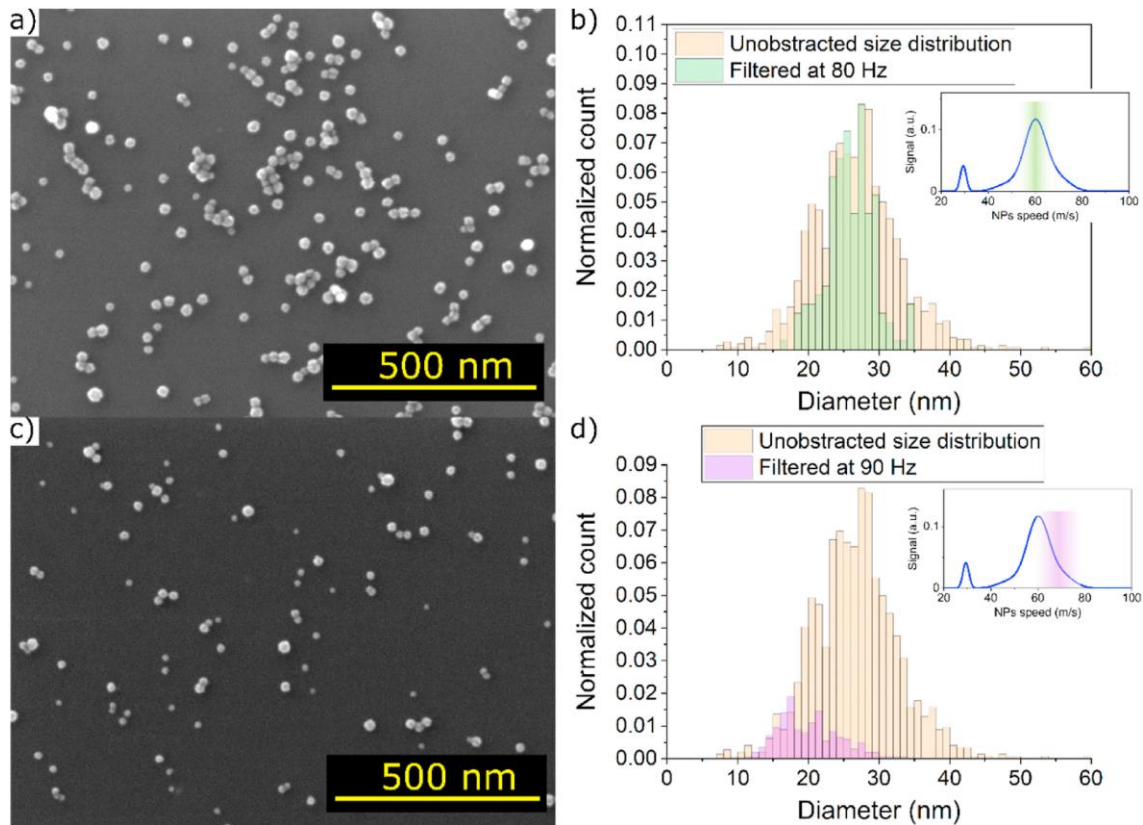


Figure 22: SEM micrographs (a, c) and size distributions (b, d) of NPs filtered at rotor frequency a, b: 80 Hz and c, d: 90 Hz for pressure in the aggregation chamber 50 Pa and magnetron current 100 mA. The size distributions are compared to the unfiltered size distribution. Since all big NPs have been filtered out, they are not shown in the distribution (they were still present in the unfiltered sample just as in Figure 20). The small insertion plots show approximately where the filtration occurred on the velocity plot. Reproduced from [PS 6].

The filtration at 29 m/s successfully removed most of the small NPs reducing their number relative to the big ones by several orders, see Figure 23. This set of experiments confirm the above-mentioned theory and proves that the mechanical time-of-flight filter may be used not only as a measuring instrument, but also as a mass filter of neutral (and charged) NPs.

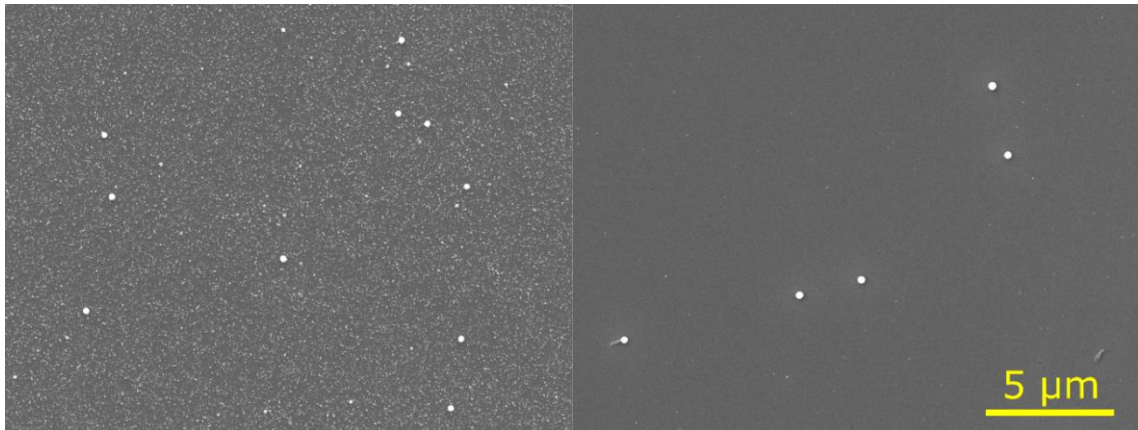


Figure 23: SEM micrographs of the unfiltered beam (left) and filtered beam with mean filtered speed of 29 m/s corresponding to the big NPs (right).

4.4 Dependency of nanoparticles speed on deposition chamber pressure

As shown in Figure 19, the pressure in the aggregation chamber is a key parameter that influences the speed of NPs exiting the gas aggregation source. It is, however, also a key parameter that influences the formation of the NPs. In some cases, e.g. for in-flight coating of the NPs or deposition of plasma polymer NPs, it is highly useful to have some other means of controlling NPs speed without changing NPs formation conditions. This possibility is offered by the variation of the pressure in the deposition chamber outside the gas aggregation source. The increase of pressure in the deposition chamber causes the NPs leaving the orifice to experience aerodynamic drag that makes them slow down. While this method allows only a decrease in speed, it is very useful in many situations as described in [PS 6].

The deceleration depends on the trajectory length and density (pressure) of the gas. The example of deceleration is presented in Figure 24. As described in [PS 6], the simple theory of Stokes drag suggests that the loss of speed should be linear. That seems to be true in the early stages of deceleration (up to 1 Pa, in Figure 24), but then it deviates. Up to about 1 Pa, the deposition rate is more or less constant but with the further increase of pressure it begins to decrease quickly. At the same time the mean size of the NPs starts to increase. Since the pressure in the deposition chamber has practically no effect on the processes in the aggregation chamber, it may be assumed that the size distribution of the NPs leaving the orifice is still same. However, the acceleration/deceleration is dependent on the size, as shown in [63]. Therefore, while the size distribution is the same for all deposition chamber pressures directly behind the orifice, the smaller NPs are decelerated faster than the bigger ones. From some point, they are unable to reach the substrate and they either deposit on the chamber walls or get dragged into

the pumping system. That causes an apparent increase of the mean size of the deposited NPs. So even though the smallest NPs started with the highest speed, they are the first to lose the speed completely. That is also the reason why the speed distribution becomes narrower with the increasing deposition chamber pressure as the speeds of different NPs sizes equalize (at least at the beginning).

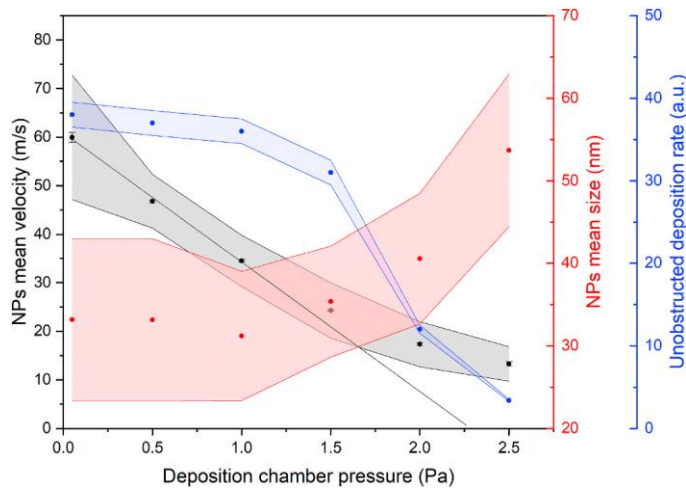


Figure 24: Dependence of the NPs velocity, size and deposition rate on the pressure in the main deposition chamber. The error bars represent the uncertainty of measurement calculated from two or more measurements and the filled area represents the full width at half maximum (FWHM) of the distribution. The black line is a linear function eye-guide connecting the first three points where all small NPs still arrive on substrate. Reproduced from [PS 6].

5 Investigation of nanoparticle reflection from substrate

When we first investigated plasma polymer NPs [24], [27], [36], we observed confusing effects during their deposition. The deposit had unusual shape, and the shape was weirdly dependent on the deposition chamber pressure. These effects were not observed for any metal NPs. At first, the effects were attributed to the aerodynamic focusing, but when the system was investigated using theoretical model described in [63], this hypothesis was rejected because the suspected forces are far too small. When we started working with composite metal/plasma polymer NPs described in [PS 4] the same effects were observed. These NPs had big metal inclusions and their density was comparable to most metal NPs. We have realized that these strange effects were in fact caused by the reflection of the NPs from the substrate upon the impact. An example of the deposits of sputtered-nylon plasma polymer NPs prepared at different deposition chamber pressures is shown in Figure 25 along with SEM micrographs of the deposits and QCM measurement of the deposition rate.

Unlike with metal NPs, the deposition is weak at low deposition chamber pressures. The deposition rate at low deposition chamber pressure is dependent on the NPs type, size and conditions inside the aggregation chamber. Under some circumstances, the deposition rate may be as low as zero even when the NPs beam is very strong. With the increase of the deposition chamber pressure, the deposition rate increases until it reaches a maximum and then decays similarly to metal NPs [PS 7]. This observation was originally the reason for the aerodynamic focusing hypothesis. However, the real reason for this behavior lies in the mechanical properties of the plasma polymer and in the speed of the NPs upon impact. The plasma polymer is a highly crosslinked organic substance, somewhat reminiscent of rubber. When the NPs leave the orifice, they acquire high speeds, usually in the tens of meters per second. Lighter NPs (plasma polymer has low mass density compared to metal) are accelerated to even higher speeds. Therefore, the plasma polymer NPs behave as fast rubber balls hitting the substrate. On nano level, every surface is slightly sticky because of the van der Waals forces. That means that there are two forces competing with each other during the impact. One is the repulsive spring force, that is dependent on the material properties and is proportional to the impact speed. The other one is the attractive van der Waals force dependent on the substrate material. The spring force may be diminished by the decrease of speed of the impacting nanoparticle. An analogy of a tennis ball hitting a Velcro wall may be used to better imagine the process. As mentioned in the previous chapter, the speed of nanoparticles may be reduced by their interaction with the gas in the deposition chamber. So, the proper explanation of the measurement presented in Figure 25 is as follows: The speed (blue dots) must be reduced under a certain level to promote NPs sticking to the surface – that is responsible for the initial deposition rate increase with rising deposition chamber pressure. At the deposition chamber pressure about 1.5 Pa the deposition rate reaches maximum and begins to fall down. This decrease is related to the loss of smallest NPs whose speed is reduced the fastest and which are no longer able to reach the substrate. With further increase of the pressure, bigger and bigger NPs are slowed down and unable to reach the substrate, as described in chapter 4.4.

In the case presented in Figure 25 the deposition rate does not decrease monotonously, but there is a secondary peak at about 4.5 Pa. The reason for its presence may be found on the SEM images. At pressures above 3 Pa, a population of big particles emerges. Up to this pressure, the big particles were too fast to deposit at all and because of their size, they required strong deceleration to decrease their speed below the deposition level.

The deposition rate in Figure 25 was measured in two ways. First during the increase of pressure (the black line which is described above and is denoted as “pressure up”) and then

during the decrease of pressure (red line denoted as “pressure down”) measured just after the “pressure up”. The “pressure down” measurement is somewhat more complicated. At the high deposition chamber pressure end, the trend is similar to the previous case. As the pressure decreases, the speed of the incoming NPs increases, but this time the QCM is covered with deposit of loosely bound NPs including the big ones (whose adhesion may be even lower than in the case of the small NPs). That causes the deposition rate to become unstable at lower deposition chamber pressures, sharply decreasing from about 2 Pa down and even becoming negative from about 1 Pa down due to the sputtering of the previous deposit by impacting energetic NPs.

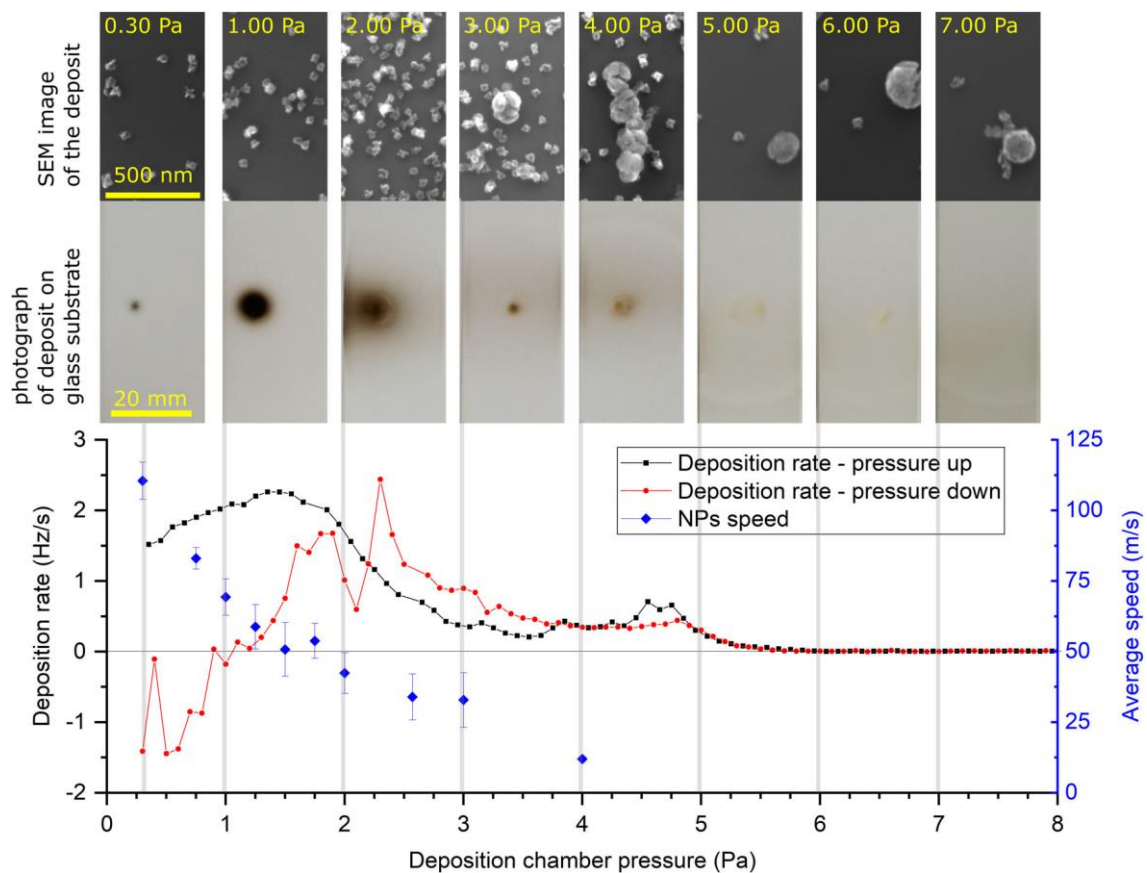


Figure 25: Deposition rate of the plasma polymer nanoparticles (pp-NPs) on a smooth substrate and their average speed as a function of the deposition chamber pressure. The plot shows a quantitative measurement using quartz crystal microbalance (QCM) (starting with a clean quartz crystal for pressure up measurement and continued with collected deposit on the crystal for pressure down measurement). For selected deposition chamber pressures (gray lines in the plot), scanning electron microscope (SEM) micrographs of NPs deposited on a smooth silicon substrate (variable deposition time) as well as photographs of deposits on a smooth glass slide (2 min deposition time) are presented. Reproduced from [PS 7].

To obtain a direct proof of the NPs reflection, we investigated the reflected beam. The schematics and the results of the experiment are shown in Figure 26. We were able to detect the reflected beam and to measure its speed spectrum. Compared to the NPs speeds in the

primary beam, the reflected NPs are much slower. That was expected since every impact leads to some loss of energy due to inelastic processes. With known speed before and after the impact it is possible to calculate the coefficient of restitution which is a measure of elasticity of the collision. With the mean speed of the NPs 117 m/s before impact and 25 m/s after impact, the coefficient of restitution is 0.21.

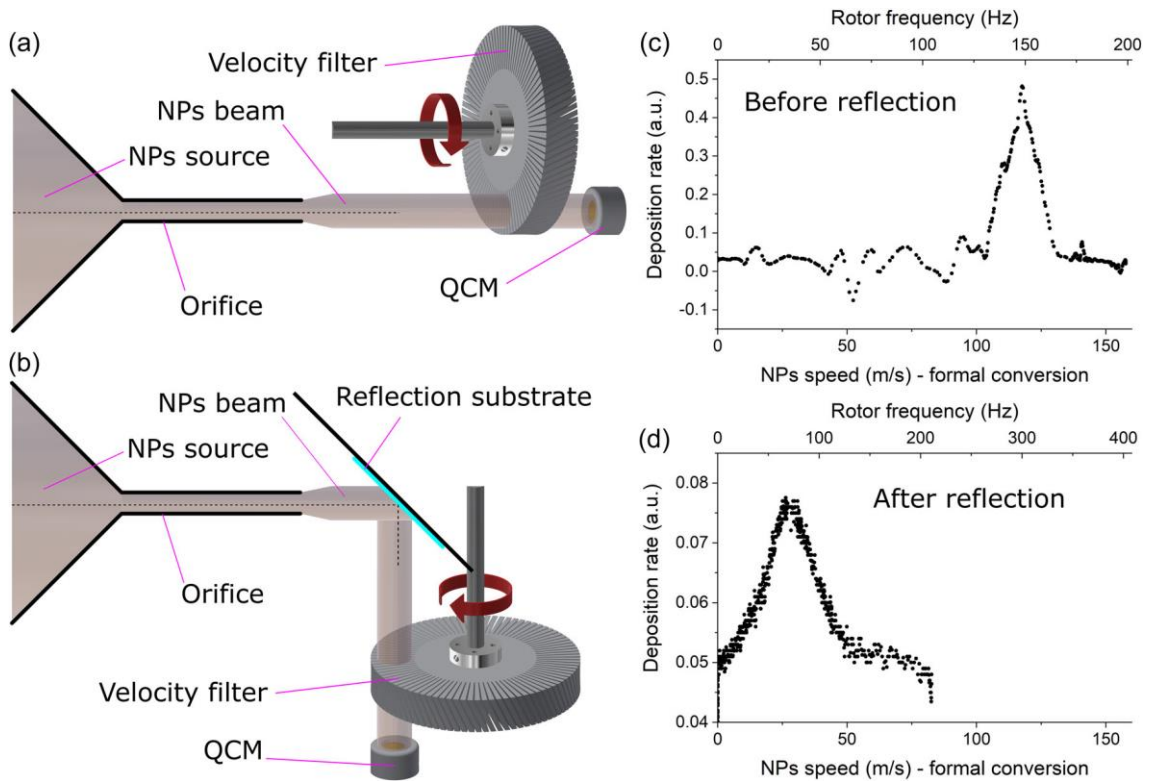


Figure 26: (a, b) Schematics of the measurement of NPs speed before and after the reflection from the substrate; (c, d) speed measurement results before and after the reflection from the glass substrate at deposition chamber pressure 0.3 Pa. The measurement was done after the nanoparticle film formed on the reflection substrate and the deposition rate of the reflected NPs reached stable value as will be discussed further. To reduce noise, the quartz crystal microbalance (QCM) data were smoothed over 20 values for both measurements. Reproduced from [PS 7].

If the reflection of the nanoparticle leads to the loss of its energy (speed), then it may be used as an alternative approach to improve sticking of the NPs to the substrate. This proved to be the correct assumption. The example of the NPs deposit in the direct and reflected beam is shown in Figure 27. In the primary beam there are no big particles that, as explained above, were too fast to deposit on the substrate. However, these are detected in the reflected beam as their speed was reduced below necessary limit.

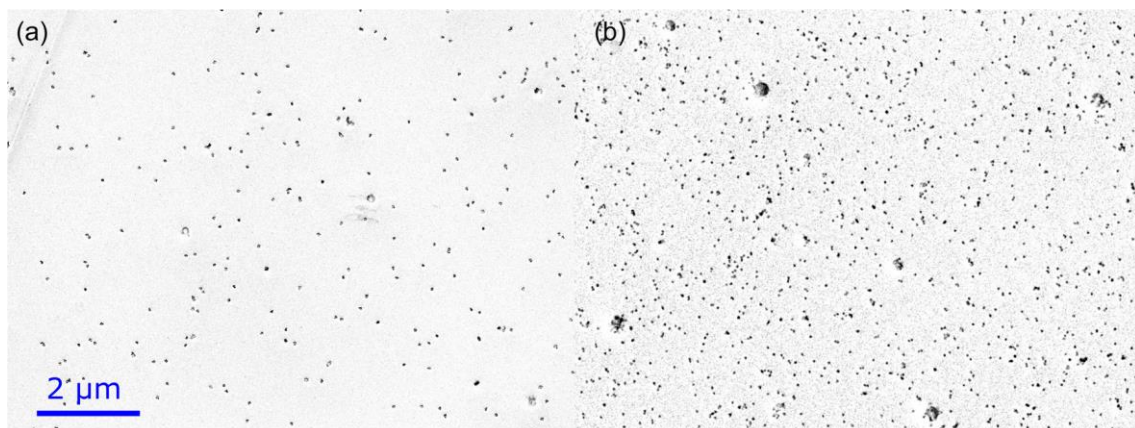


Figure 27: SEM micrographs (negative for better visibility of nylon NPs): (a) directly deposited; (b) deposited after reflection from the glass substrate. Common deposition condition: aggregation chamber pressure 50 Pa, RF power 60 W, orifice-substrate distance 18 cm, deposition chamber pressure 0.3 Pa. Reproduced from [PS 7].

The effect of the energy loss after the reflection may be used even more effectively with the use of structured substrates such as fiber fabrics. The idea is depicted in Figure 28c. Unless the nanoparticle hits the very top of some top layer fiber, there is a very good chance it would undergo multiple collisions with the substrate (fibers) eventually losing enough energy to stick to some fiber. Figure 28 also shows SEM images of the NPs deposit on a silicon substrate and on a single fiber of carbon fiber fabric. On the carbon fiber fabric, we can again see the presence of the big NPs. It should be noted that the big NPs were not present on every fiber, but only on those that had suitable position to collect the reflected NPs.

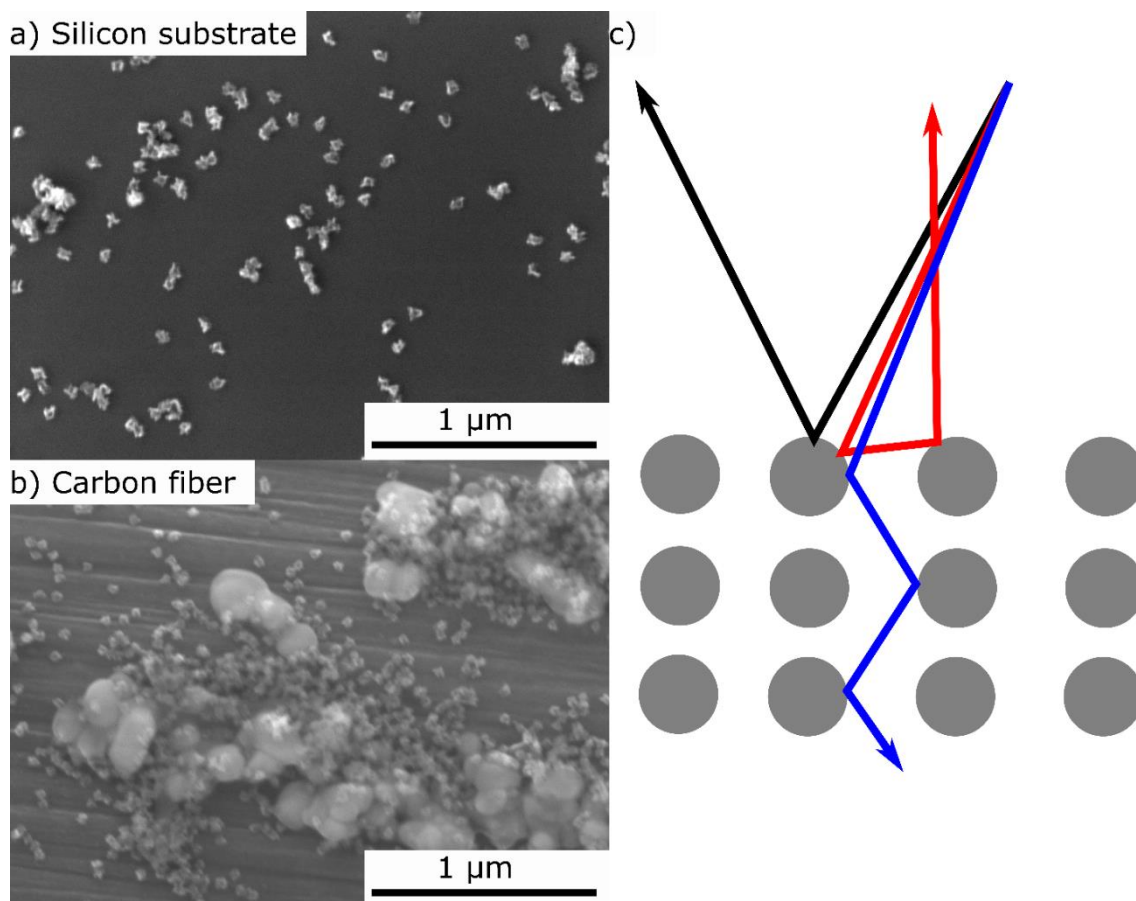


Figure 28: a) NPs deposited on a smooth silicon substrate; b) NPs deposited on a carbon fiber fabric (the background of the image is a single fiber; the big NPs were present only on some fibers); c) schematics of NPs (arrows) penetration through fibers (grey circles) in the fiber fabric. Reproduced from [PS 7].

In order to investigate the efficiency of the NPs capture on different substrates, we have constructed a special substrate holder shown in Figure 29a. Glass, different types of fiber fabrics and a liquid (vacuum grease) spread on a glass slide were used as a reflection substrate. The deposition substrate was either the QCM to measure the amount of the incoming reflected NPs or a glass fiber fabric to visualize the deposit. The deposition substrate was shielded from the primary beam by a shield. However, this was just additional safety feature since the primary beam was already too narrow to hit the reflection substrate. As shown in Figure 29b,c,e, the strongest reflected beam came from the glass substrate because it was hard and smooth. The fiber fabrics produced an attenuated beam whose intensity was dependent on the fabric thickness and structure. But even though the reflection was highly suppressed, it was still measurable. In the search for a substrate that would be able to capture all incoming NPs we investigated liquid substrates. We tested two liquids: polyethylene glycol (PEG) and vacuum grease. Both were highly efficient in capturing the NPs, but since the PEG had noticeable vapor

tension, it interfered with the QCM measurements and therefore in the publication [PS 7] we settled only for the vacuum grease.

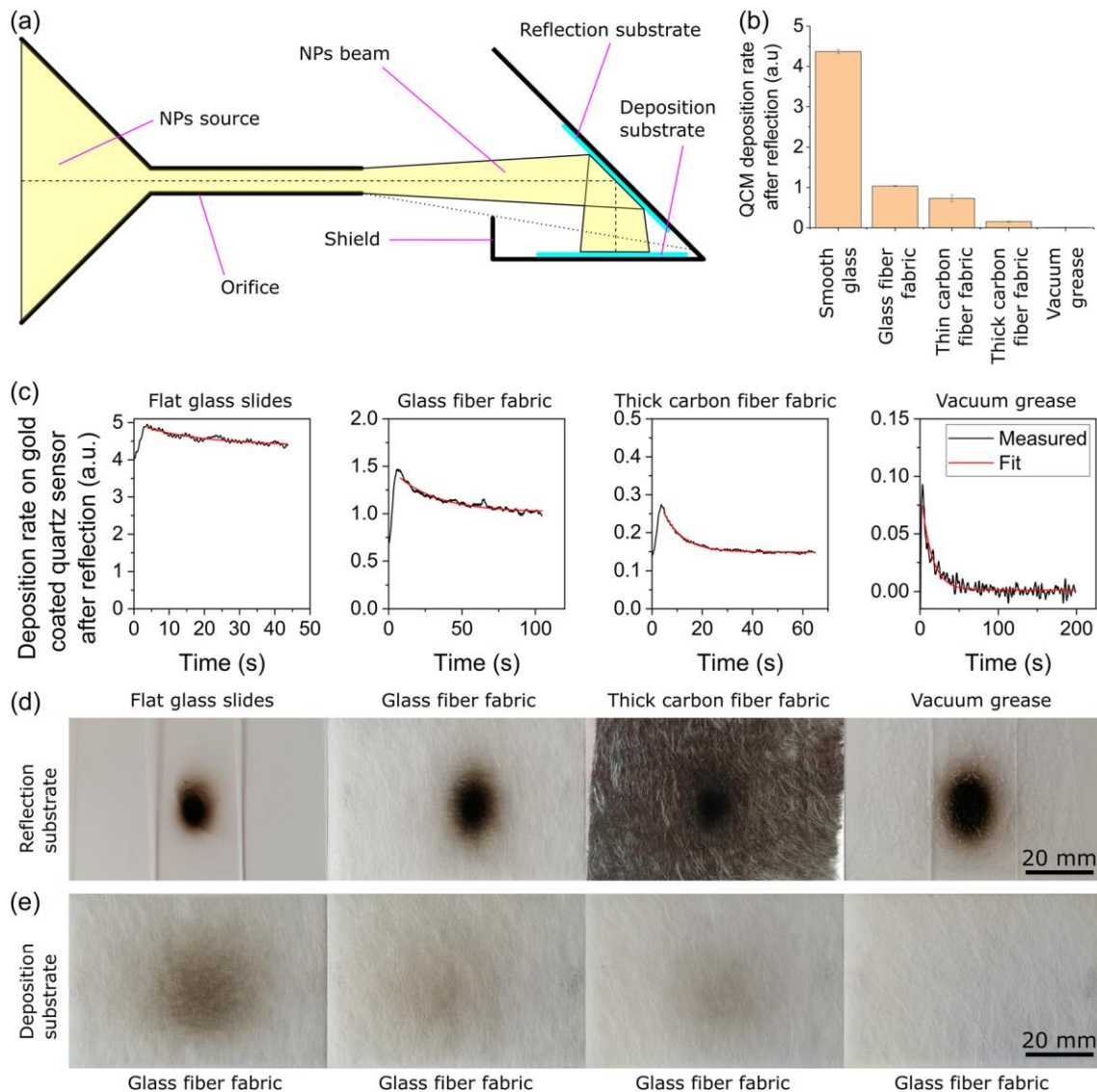


Figure 29: (a) Schematics of substrate holder to investigate reflection of nanoparticles from different substrates; (b) asymptotic values of deposition rate after reflection from different substrates; (c) time-resolved deposition rates after the reflection from different substrates; (d, e) photographs of the reflection and deposition substrates after 10 min of deposition. Reproduced from [PS 7].

The deposition rates of the reflected NPs shown in Figure 29b are the steady state values. The time-resolved measurements are shown in Figure 29c. In all cases, there is a signal build-up (most likely due to the reaction time of the QCM sensor) followed by the exponential decay towards the non-zero value (except for the liquid substrates). This decay is caused by the growth of the nanoparticles film on the reflection substrate that attenuates the reflection, as it makes the substrate rougher.

6 Conclusions

In this work, several methods for preparation of composite nanoparticles using a gas aggregation source are presented, followed by the description of the measurement of nanoparticles speed which is used to explain the nanoparticle-substrate interaction during the deposition process.

In the first study we describe how to produce composite nanoparticles from a very simple setup using a magnetron target made of copper with tungsten pellets set into the erosion track. It was demonstrated that depending on the nanoparticles' composition, the nanoparticles are to different degree prone to be trapped in the plasma near the magnetron target. To better understand the nanoparticle formation processes, in-situ calorimetric measurements were performed on the pure copper, copper/tungsten and pure tungsten and main heating mechanisms were described.

The next study investigated the deposition of composite NPs from two perpendicular magnetrons in one aggregation chamber in arrow configuration to obtain more advanced control over the core and shell formation. The conditions for the deposition of core shell NPs without admixture of single-phase NPs were identified. The last investigated system of composite nanoparticles used an organic admixture to the working gas during the RF sputtering of a metal target which led to the successful production of multicore/shell metal/plasma polymer nanoparticles with high degree of control over their composition.

This study was followed by investigation of nanoparticles speed necessary to explain the nanoparticle-substrate interaction effects observed for plasma polymer nanoparticles. For this purpose, a mechanical time-of-flight filter has been constructed. It is capable of measurement of nanoparticles speeds regardless of whether the nanoparticles are charged or not. Because the nanoparticle speed was found to be dependent on its size, the filter was also successfully used as a mass filter.

With measured nanoparticle speeds, we were able to explain strange effects related to the deposition of plasma polymer nanoparticles and composite nanoparticles containing plasma polymer. It was found that these nanoparticles behave as rubber balls and reflect from substrate when they hit it with too high speed. The reflection was studied in detail and several methods to prevent it and to promote the deposition on substrate have been described.

7 References

- [1] C. Dhand *et al.*, "Methods and strategies for the synthesis of diverse nanoparticles and their applications: a comprehensive overview," *RSC Adv.*, vol. 5, no. 127, pp. 105003–105037, 2015, doi: 10.1039/C5RA19388E.
- [2] I. Khan, K. Saeed, and I. Khan, "Nanoparticles: Properties, applications and toxicities," *Arab. J. Chem.*, vol. 12, no. 7, pp. 908–931, Nov. 2019, doi: 10.1016/j.arabjc.2017.05.011.
- [3] T. Xing *et al.*, "Ball milling: a green mechanochemical approach for synthesis of nitrogen doped carbon nanoparticles," *Nanoscale*, vol. 5, no. 17, p. 7970, 2013, doi: 10.1039/c3nr02328a.
- [4] S. Horikoshi and N. Serpone, "In-liquid plasma: a novel tool in the fabrication of nanomaterials and in the treatment of wastewaters," *RSC Adv.*, vol. 7, no. 75, pp. 47196–47218, 2017, doi: 10.1039/C7RA09600C.
- [5] M. A. Bratescu, S.-P. Cho, O. Takai, and N. Saito, "Size-Controlled Gold Nanoparticles Synthesized in Solution Plasma," *J. Phys. Chem. C*, vol. 115, no. 50, pp. 24569–24576, Dec. 2011, doi: 10.1021/jp207447c.
- [6] Y. Fukui *et al.*, "Preparation of monodispersed polyelectrolyte microcapsules with high encapsulation efficiency by an electrospray technique," *Colloids Surfaces A Physicochem. Eng. Asp.*, vol. 370, no. 1–3, pp. 28–34, Nov. 2010, doi: 10.1016/j.colsurfa.2010.08.039.
- [7] S. Ghayempour and S. M. Mortazavi, "Fabrication of micro–nanocapsules by a new electrospraying method using coaxial jets and examination of effective parameters on their production," *J. Electrostat.*, vol. 71, no. 4, pp. 717–727, Aug. 2013, doi: 10.1016/j.elstat.2013.04.001.
- [8] J. Anu Bhushani and C. Anandharamakrishnan, "Electrospinning and electrospraying techniques: Potential food based applications," *Trends Food Sci. Technol.*, vol. 38, no. 1, pp. 21–33, Jul. 2014, doi: 10.1016/j.tifs.2014.03.004.
- [9] W. Y. Teoh, R. Amal, and L. Mädler, "Flame spray pyrolysis: An enabling technology for nanoparticles design and fabrication," *Nanoscale*, vol. 2, no. 8, p. 1324, 2010, doi: 10.1039/c0nr00017e.
- [10] A. Vasudevan *et al.*, "From faceted nanoparticles to nanostructured thin film by plasma-jet redox reaction of ionic gold," *J. Alloys Compd.*, vol. 928, p. 167155, Dec. 2022, doi:

10.1016/j.jallcom.2022.167155.

- [11] A. Bjelajac *et al.*, "Gold nanoparticles synthesis and immobilization by atmospheric pressure DBD plasma torch method," *Nanoscale Adv.*, vol. 5, no. 9, pp. 2573–2582, 2023, doi: 10.1039/D3NA00007A.
- [12] J. He, X. Wen, L. Wu, H. Chen, J. Hu, and X. Hou, "Dielectric barrier discharge plasma for nanomaterials: Fabrication, modification and analytical applications," *TrAC Trends Anal. Chem.*, vol. 156, p. 116715, Nov. 2022, doi: 10.1016/j.trac.2022.116715.
- [13] B. Gojdka, V. Hrkac, T. Strunskus, V. Zaporojtchenko, L. Kienle, and F. Faupel, "Study of cobalt clusters with very narrow size distribution deposited by high-rate cluster source," *Nanotechnology*, vol. 22, no. 46, p. 465704, Nov. 2011, doi: 10.1088/0957-4484/22/46/465704.
- [14] M. Drábik *et al.*, "Morphology of Titanium Nanocluster Films Prepared by Gas Aggregation Cluster Source," *Plasma Process. Polym.*, vol. 8, no. 7, pp. 640–650, Jul. 2011, doi: 10.1002/ppap.201000126.
- [15] O. Polonskyi *et al.*, "Nanocomposite metal/plasma polymer films prepared by means of gas aggregation cluster source," *Thin Solid Films*, vol. 520, no. 12, pp. 4155–4162, Apr. 2012, doi: 10.1016/j.tsf.2011.04.100.
- [16] K. Sattler, J. Mühlbach, and E. Recknagel, "Generation of Metal Clusters Containing from 2 to 500 Atoms," *Phys. Rev. Lett.*, vol. 45, no. 10, pp. 821–824, Sep. 1980, doi: 10.1103/PhysRevLett.45.821.
- [17] H. Haberland, M. Karrais, and M. Mall, "A new type of cluster and cluster ion source," *Zeitschrift für Phys. D Atoms, Mol. Clust.*, vol. 20, no. 1–4, pp. 413–415, Mar. 1991, doi: 10.1007/BF01544025.
- [18] H. Haberland, M. Karrais, M. Mall, and Y. Thurner, "Thin films from energetic cluster impact: A feasibility study," *J. Vac. Sci. Technol. A Vacuum, Surfaces, Film.*, vol. 10, no. 5, pp. 3266–3271, Sep. 1992, doi: 10.1116/1.577853.
- [19] P. Solar, O. Polonskyi, A. Choukourov, A. Artemenko, H. Biederman, and D. Slavinska, "Nanostructured and nanocluster thin films," 2010.
- [20] M. Drabik *et al.*, "Aging of nanocluster Ti/TiO_x films prepared by means of gas aggregation cluster source," *Surf. Coatings Technol.*, vol. 205, pp. S48–S52, 2011, doi: 10.1016/j.surfcoat.2011.02.013.

- [21] O. Kylián *et al.*, “Deposition of Pt nanoclusters by means of gas aggregation cluster source,” *Mater. Lett.*, vol. 79, pp. 229–231, 2012, doi: 10.1016/j.matlet.2012.04.022.
- [22] W. A. Heer and P. Milani, “An improved laser vaporization cluster source and time-of-flight mass spectrometer,” *Zeitschrift für Phys. D Atoms, Mol. Clust.*, vol. 20, no. 1–4, pp. 437–439, Mar. 1991, doi: 10.1007/BF01544031.
- [23] G. Ganteför, H. R. Siekmann, H. O. Lutz, and K. H. Meiwes-Broer, “Pure metal and metal-doped rare-gas clusters grown in a pulsed ARC cluster ion source,” *Chem. Phys. Lett.*, vol. 165, no. 4, pp. 293–296, Jan. 1990, doi: 10.1016/0009-2614(90)87191-S.
- [24] O. Polonskyi *et al.*, “Nylon-sputtered nanoparticles: fabrication and basic properties,” *J. Phys. D. Appl. Phys.*, vol. 45, no. 49, p. 495301, Dec. 2012, doi: 10.1088/0022-3727/45/49/495301.
- [25] O. Kylián *et al.*, “Control of Wettability of Plasma Polymers by Application of Ti Nano-Clusters,” *Plasma Process. Polym.*, vol. 9, no. 2, pp. 180–187, Feb. 2012, doi: 10.1002/ppap.201100113.
- [26] O. Polonskyi *et al.*, “Deposition of Al nanoparticles and their nanocomposites using a gas aggregation cluster source,” *J. Mater. Sci.*, vol. 49, no. 9, pp. 3352–3360, May 2014, doi: 10.1007/s10853-014-8042-5.
- [27] P. Solař *et al.*, “Nanostructured thin films prepared from cluster beams,” *Surf. Coatings Technol.*, vol. 205, pp. S42–S47, 2011, doi: 10.1016/j.surfcoat.2011.01.059.
- [28] P. Solař *et al.*, “Particles induced surface nanoroughness of titanium surface and its influence on adhesion of osteoblast-like MG-63 cells,” *Appl. Surf. Sci.*, vol. 324, pp. 99–105, Jan. 2015, doi: 10.1016/j.apsusc.2014.10.082.
- [29] P. Solař *et al.*, “Nanocomposite coatings of Ti/C:H plasma polymer particles providing a surface with variable nanoroughness,” *Surf. Coatings Technol.*, vol. 206, no. 21, pp. 4335–4342, Jun. 2012, doi: 10.1016/j.surfcoat.2012.02.005.
- [30] A. M. Ahadi, V. Zaporojtchenko, T. Peter, O. Polonskyi, T. Strunskus, and F. Faupel, “Role of oxygen admixture in stabilizing TiO_x nanoparticle deposition from a gas aggregation source,” *J. Nanoparticle Res.*, vol. 15, no. 12, p. 2125, Dec. 2013, doi: 10.1007/s11051-013-2125-0.
- [31] T. Peter, S. Rehders, U. Schürmann, T. Strunskus, V. Zaporojtchenko, and F. Faupel, “High rate deposition system for metal-cluster/SiO_xC_yH_z-polymer nanocomposite thin

- films," *J. Nanoparticle Res.*, vol. 15, no. 6, p. 1710, Jun. 2013, doi: 10.1007/s11051-013-1710-6.
- [32] T. Peter *et al.*, "Influence of reactive gas admixture on transition metal cluster nucleation in a gas aggregation cluster source," *J. Appl. Phys.*, vol. 112, no. 11, Dec. 2012, doi: 10.1063/1.4768528.
- [33] O. Polonskyi *et al.*, "Huge increase in gas phase nanoparticle generation by pulsed direct current sputtering in a reactive gas admixture," *Appl. Phys. Lett.*, vol. 103, no. 3, Jul. 2013, doi: 10.1063/1.4816036.
- [34] A. Shelemin *et al.*, "Preparation of metal oxide nanoparticles by gas aggregation cluster source," *Vacuum*, vol. 120, pp. 162–169, Oct. 2015, doi: 10.1016/j.vacuum.2015.07.008.
- [35] M. Drábik *et al.*, "Deposition of Fluorocarbon Nanoclusters by Gas Aggregation Cluster Source," *Plasma Process. Polym.*, vol. 9, no. 4, pp. 390–397, Apr. 2012, doi: 10.1002/ppap.201100147.
- [36] P. Solař *et al.*, "Nylon-sputtered plasma polymer particles produced by a semi-hollow cathode gas aggregation source," *Vacuum*, vol. 111, pp. 124–130, Jan. 2015, doi: 10.1016/j.vacuum.2014.09.023.
- [37] A. Shelemin *et al.*, "Cycling instabilities in a gas aggregation cluster source used for plasma polymer nanoparticle fabrication," *NANOCON 2017 - Conf. Proceedings, 9th Int. Conf. Nanomater. - Res. Appl.*, vol. 2017-October, pp. 765–770, 2018.
- [38] A. Shelemin *et al.*, "Formation of organosilicon nanoparticles in a gas aggregation source as witnessed by in situ light scattering," *NANOCON 2017 - Conf. Proceedings, 9th Int. Conf. Nanomater. - Res. Appl.*, vol. 2017-October, pp. 937–941, 2018.
- [39] J. Hanuš *et al.*, "Fabrication of Ni@Ti core-shell nanoparticles by modified gas aggregation source," *J. Phys. D: Appl. Phys.*, vol. 50, no. 47, p. 475307, Nov. 2017, doi: 10.1088/1361-6463/aa8f25.
- [40] O. Kylián, J. Kratochvíl, J. Hanuš, O. Polonskyi, P. Solař, and H. Biederman, "Fabrication of Cu nanoclusters and their use for production of Cu/plasma polymer nanocomposite thin films," *Thin Solid Films*, vol. 550, pp. 46–52, Jan. 2014, doi: 10.1016/j.tsf.2013.10.029.
- [41] T. Acsente *et al.*, "Synthesis of flower-like tungsten nanoparticles by magnetron sputtering combined with gas aggregation," *Eur. Phys. J. D*, vol. 69, no. 6, p. 161, Jun. 2015, doi: 10.1140/epjd/e2015-60097-4.

- [42] T. Raghu, R. Sundaresan, P. Ramakrishnan, and T. R. Rama Mohan, "Synthesis of nanocrystalline copper–tungsten alloys by mechanical alloying," *Mater. Sci. Eng. A*, vol. 304–306, no. 1–2, pp. 438–441, May 2001, doi: 10.1016/S0921-5093(00)01444-1.
- [43] A. Shelemin *et al.*, "Nucleation and Growth of Magnetron-Sputtered Ag Nanoparticles as Witnessed by Time-Resolved Small Angle X-Ray Scattering," *Part. Part. Syst. Charact.*, vol. 37, no. 2, p. 1900436, Feb. 2020, doi: 10.1002/ppsc.201900436.
- [44] J. Kousal *et al.*, "Magnetron-sputtered copper nanoparticles: lost in gas aggregation and found by in situ X-ray scattering," *Nanoscale*, vol. 10, no. 38, pp. 18275–18281, 2018, doi: 10.1039/C8NR06155F.
- [45] J. Goree, "Charging of particles in a plasma," *Plasma Sources Sci. Technol.*, vol. 3, no. 3, pp. 400–406, Aug. 1994, doi: 10.1088/0963-0252/3/3/025.
- [46] T. Acsente, M. C. Istrate, V. Satulu, B. Bitu, and G. Dinescu, "Operation of a magnetron sputtering gas aggregation cluster source in a plasma jet regime for synthesis of core–shell nanoparticles," *J. Phys. D. Appl. Phys.*, vol. 54, no. 2, p. 02LT01, Jan. 2021, doi: 10.1088/1361-6463/abbb05.
- [47] T. Košutová *et al.*, "In-flight coating of Ag nanoparticles with Cu," *J. Phys. D. Appl. Phys.*, vol. 54, no. 1, p. 015302, Jan. 2021, doi: 10.1088/1361-6463/abb847.
- [48] T. Kretková *et al.*, "In-flight modification of Ni nanoparticles by tubular magnetron sputtering," *J. Phys. D. Appl. Phys.*, vol. 52, no. 20, p. 205302, May 2019, doi: 10.1088/1361-6463/ab00d0.
- [49] H. Libenská *et al.*, "Core @ shell Ag @ Ti Nanoparticles Prepared by In-flight Coating," in *WDS20*, 2020, pp. 118–122.
- [50] O. Kylián *et al.*, "Core@shell Cu/hydrocarbon plasma polymer nanoparticles prepared by gas aggregation cluster source followed by in-flight plasma polymer coating," *Plasma Process. Polym.*, vol. 15, no. 1, p. 1700109, Jan. 2018, doi: 10.1002/ppap.201700109.
- [51] L. Martínez, M. Díaz, E. Román, M. Ruano, D. Llamosa P., and Y. Huttel, "Generation of Nanoparticles with Adjustable Size and Controlled Stoichiometry: Recent Advances," *Langmuir*, vol. 28, no. 30, pp. 11241–11249, 2012, doi: 10.1021/la3022134.
- [52] L. Martínez, A. Mayoral, M. Espiñeira, E. Roman, F. J. Palomares, and Y. Huttel, "Core@shell, Au@TiO_x nanoparticles by gas phase synthesis," *Nanoscale*, vol. 9, no. 19, pp. 6463–6470, 2017, doi: 10.1039/C7NR01148B.

- [53] E. Palesch *et al.*, “Mechanical stability of titanium and plasma polymer nanoclusters in nanocomposite coatings,” *Thin Solid Films*, vol. 544, pp. 593–596, Oct. 2013, doi: 10.1016/j.tsf.2012.12.060.
- [54] M. Ganeva, P. V. Kashtanov, A. V. Kosarim, B. M. Smirnov, and R. Hippler, “Clusters as a diagnostics tool for gas flows,” *Physics-Uspekhi*, vol. 58, no. 6, pp. 579–588, Jun. 2015, doi: 10.3367/UFNe.0185.201506d.0619.
- [55] C. Binns, “Nanoclusters deposited on surfaces,” *Surf. Sci. Rep.*, vol. 44, no. 1–2, pp. 1–49, Oct. 2001, doi: 10.1016/S0167-5729(01)00015-2.
- [56] J. A. Simpson, “Design of Retarding Field Energy Analyzers,” *Rev. Sci. Instrum.*, vol. 32, no. 12, pp. 1283–1293, Dec. 1961, doi: 10.1063/1.1717235.
- [57] J. G. DASH and H. S. SOMMERS, “A High Transmission Slow Neutron Velocity Selector,” *Rev. Sci. Instrum.*, vol. 24, no. 2, pp. 91–96, Mar. 1953, doi: 10.1088/0950-7671/25/3/108.
- [58] R. C. Miller and P. Kusch, “Velocity Distributions in Potassium and Thallium Atomic Beams,” *Phys. Rev.*, vol. 99, no. 4, pp. 1314–1321, Aug. 1955, doi: 10.1103/PhysRev.99.1314.
- [59] H. U. Hostettler and R. B. Bernstein, “Improved Slotted Disk Type Velocity Selector for Molecular Beams,” *Rev. Sci. Instrum.*, vol. 31, no. 8, pp. 872–877, Aug. 1960, doi: 10.1063/1.1717075.
- [60] R. van Steyn and N. F. Verster, “The design of slotted disc velocity selectors for molecular beams,” *J. Phys. E.*, vol. 5, no. 7, pp. 691–697, 1972, doi: 10.1088/0022-3735/5/7/027.
- [61] D. R. Frankl, “Effects of angular beam dispersion on performance of slotted-disk velocity selectors,” *Rev. Sci. Instrum.*, vol. 45, no. 11, pp. 1375–1377, Nov. 1974, doi: 10.1063/1.1686505.
- [62] F. Pirani *et al.*, “A simple and compact mechanical velocity selector of use to analyze/select molecular alignment in supersonic seeded beams,” *Rev. Sci. Instrum.*, vol. 75, no. 2, pp. 349–354, Feb. 2004, doi: 10.1063/1.1637433.
- [63] J. Kousal *et al.*, “Characterization of nanoparticle flow produced by gas aggregation source,” *Vacuum*, vol. 96, pp. 32–38, Oct. 2013, doi: 10.1016/j.vacuum.2013.02.015.
- [64] L. Zhang, J. Shao, and X. Chen, “CFD simulation of nozzle characteristics in a gas

aggregation cluster source," *Vacuum*, vol. 129, pp. 105–110, Jul. 2016, doi: 10.1016/j.vacuum.2016.04.020.

- [65] B. M. Smirnov, I. Shyjumon, and R. Hippler, "Flow of nanosize cluster-containing plasma in a magnetron discharge," *Phys. Rev. E*, vol. 75, no. 6, p. 066402, Jun. 2007, doi: 10.1103/PhysRevE.75.066402.

8 List of commented publications

[PS 1] P. Solař, D. Nikitin, J. Hanuš, O. Kylián, M. Vaidulych, H. Biederman, Production of heterogeneous copper-tungsten particles, in: NANOCON 2017, 9th Int. Conf. Nanomater. - Res. Appl., 2017: pp. 16–21.

[PS 2] S. Gauter, F. Haase, P. Solař, O. Kylián, P. Kúš, A. Choukourov, H. Biederman, H. Kersten, Calorimetric investigations in a gas aggregation source, J. Appl. Phys. 124 (2018) 073301. <https://doi.org/10.1063/1.5037413>.

[PS 3] P. Solař, J. Hanuš, M. Cieslar, T. Košutová, K. Škorvánková, O. Kylián, P. Kúš, H. Biederman, Composite Ni@Ti nanoparticles produced in arrow-shaped gas aggregation source, J. Phys. D: Appl. Phys. 53 (2020). <https://doi.org/10.1088/1361-6463/ab7353>.

[PS 4] P. Solař, O. Polonskyi, A. Olbricht, A. Hinz, A. Shelemin, O. Kylián, A. Choukourov, F. Faupel, H. Biederman, Single-step generation of metal-plasma polymer multicore@shell nanoparticles from the gas phase, Sci. Rep. 7 (2017) 8514. <https://doi.org/10.1038/s41598-017-08274-6>.

[PS 5] P. Solař, J. Kousal, J. Hanuš, K. Škorvánková, A. Kuzminova, O. Kylián, Mechanical time-of-flight filter based on slotted disks and helical rotor for measurement of velocities of nanoparticles, Sci. Rep. 11 (2021) 6415. <https://doi.org/10.1038/s41598-021-85533-7>.

[PS 6] P. Solař, K. Škorvánková, A. Kuzminova, J. Kousal, O. Kylián, Measurement of velocities of copper nanoparticles exiting a gas aggregation source, Vacuum. 202 (2022) 111114. <https://doi.org/10.1016/j.vacuum.2022.111114>.

[PS 7] P. Solař, K. Škorvánková, A. Kuzminova, O. Kylián, Challenges in the deposition of plasma polymer nanoparticles using gas aggregation source: Rebounding upon impact and how to land them on a substrate, Plasma Process. Polym. (2023) 1–10. <https://doi.org/10.1002/ppap.202300070>.

9 Commented publications